

5-2018

A Numerical Investigation of Bio-inspired Scaffolds and Surface Textures

Yucong Gu
University of Arkansas, Fayetteville

Follow this and additional works at: <https://scholarworks.uark.edu/etd>



Part of the [Biomechanical Engineering Commons](#), and the [Manufacturing Commons](#)

Citation

Gu, Y. (2018). A Numerical Investigation of Bio-inspired Scaffolds and Surface Textures. *Graduate Theses and Dissertations* Retrieved from <https://scholarworks.uark.edu/etd/2746>

This Thesis is brought to you for free and open access by ScholarWorks@UARK. It has been accepted for inclusion in Graduate Theses and Dissertations by an authorized administrator of ScholarWorks@UARK. For more information, please contact scholar@uark.edu, uarepos@uark.edu.

A Numerical Investigation of Bio-inspired Scaffolds and Surface Textures

A thesis submitted in partial fulfillment
of the requirements for the degree of
Master of Science in Mechanical Engineering

by

Yucong Gu
University of Kansas
Bachelor of Science in Mechanical Engineering, 2015

May 2018
University of Arkansas

This thesis is approved for recommendation to the Graduate Council.

Arun Nair, PhD
Thesis Director

Wenchao Zhou, PhD
Committee Member

Paul Millett, PhD
Committee Member

ABSTRACT

Synthetic scaffolds are widely used as implants to repair bone fracture. Without a proper design, scaffolds could pose significant health risks to the patient and fail to heal the bone properly. A good synthetic scaffold needs to have high porosity and large pore size to allow new bone cells to form on it. However, a scaffold with higher porosity and larger pore size tends to have reduced mechanical strength. Thus, it is important to find a structural design which allows the implant to have a high porosity and large pore size while retaining high strength. In this research, a 3D-printable bio-inspired structure based on the unit cell of hydroxyapatite (HAp), along with several other common scaffold structures, were designed and tested using a multiscale approach. Those structures are tested under different loading conditions to find the stress levels. HAp material properties are extracted from the density functional theory calculations, and the effect of porosity on the material properties are modeled based on empirical relations by utilizing the density as the scaling factor. The results show that the HAp-inspired scaffold could have up to 70% lower stress level when compared to other common scaffold designs, such as round or square pores scaffolds, under the same loading condition. Due to substitutions during aging, the scaffolds made of apatite can be significantly different from stoichiometric HAp. Hence, this study is also extended to test the HAp-inspired scaffold with varying anionic and cationic substitutions, including Mg^{2+} , Zn^{2+} , and CO_3^{2-} . Furthermore, the surface texture of synthetic scaffolds has also become an important research subject in the last decade. Studies have found that surface texture can alter surface properties, such as cell adhesion, protein adsorption, and coefficient of friction, of a biomaterial. In this study, two of very promising 3D-printable bio-inspired surface textures are studied for their stress reaction under a loading condition. Some advice that could lead to a structurally stronger

surface texture design is concluded. This study will provide an insight into a better scaffold design based on bio-inspired structures and the effects of substitutions on HAp scaffolds.

ACKNOWLEDGEMENTS

I would like to thank the support from my academic advisor Dr. Arun K. Nair and my colleagues in the Multiscale Materials Modeling Laboratory, each one of you have given me countless valuable and useful suggestions and advice in the process of conducting this study.

I also would like to acknowledge the support from the Department of Mechanical Engineering, the University of Arkansas and also the Arkansas High-Performance Computing Center (AHPCC), and the support provided by the Center for Advanced Surface Engineering from NSF EPSCoR IIA 1457888.

TABLE OF CONTENTS

CHAPTER 1: INTRODUCTION.....	1
1.1 Motivation for Present Research.....	1
1.2 Literature Review.....	2
1.3 Thesis Overview.....	8
CHAPTER 2: SCAFFOLD AND SURFACE TEXTURE DESIGNS.....	10
2.1 Scaffold Designs.....	10
2.2 Surface Texture Designs.....	13
CHAPTER 3: MULTISCALE MODELING METHOD.....	15
3.1 Elastic Constants of Stoichiometric HAp.....	15
3.2 Substitution Effects on the Elastic Constants of HAp.....	16
3.3 Elastic Constant Scaling.....	18
3.4 FEA Simulation Setups for Computational Models developed.....	19
CHAPTER 4: RESULTS AND DISCUSSION.....	25
4.1 Scaffold FEA Simulations.....	25
4.2 Substitution Effects.....	35
4.3 Surface Texture Simulations.....	38

CHAPTER 5: CONCLUSIONS.....	44
CHAPTER 6: FUTURE WORK.....	47
REFERENCES.....	48

LIST OF FIGURES

Figure 1.2.1.1 Schematic Hierarchical Structure of a Human Bone.....	3
Figure 1.2.2.1 A Honeycomb Sandwich Structure Illustration.....	5
Figure 2.1.1 The Atomic Configuration of HAp and Design of the HAp Inspired Scaffold.....	11
Figure 3.2.1 B-type Carbonate Substitutions for First Phosphate Groups of HAp.....	17
Figure 3.4.1.1.1 Loading Conditions for Implants.....	20
Figure 3.4.1.1.2 Scaffolds Loading Cases.....	21
Figure 3.4.1.2.1 Example of Surface Texture Simulation.....	24
Figure 4.1.1 Uniaxial Compressive Simulation Results.....	25
Figure 4.1.2 Relationship between Surface Area and Maximum Stress for Scaffolds.....	27
Figure 4.1.3 Biaxial Compressive Tests and Bending Tests Results.....	29
Figure 4.1.4 The Normal Stress Distribution of Selected Scaffold Structures.....	31
Figure 4.1.5 HAp inspired Scaffold Breakdown.....	32
Figure 4.1.6 Modified HAp inspired Model.....	34
Figure 4.2.1 Substitution Effects on Scaffolds.....	36
Figure 4.3.1 Ten-layer Structure Surfaces Simulation results.....	39
Figure 4.3.2 Stress Distribution of 10-layer Surfaces.....	40

Figure 4.3.3 Effects of Coating Thickness and Structure Density.....41

Figure 4.3.4 Effects of Number of Layers.....42

LIST OF TABLES

Table 2.1.1 List of Scaffold Structures	13
Table 2.2.1 Ideal Smooth Surface Structures	14
Table 3.4.1.1.1 Loading Conditions for Each case.....	21
Table 3.4.1.2.1: All Simulation Cases in the Surface Texture Study.....	23
Table 3.4.1.2.2 Material Property Used in Surface Texture Simulations.....	24
Table 4.2.1 DFT Calculation Results of HAp.....	35

CHAPTER 1: INTRODUCTION

1.1 Motivation for Present Research

Bone structure is one of the most important components in the body, which is required for humans to perform any mechanical movement. However, it can be vulnerable; every year, millions of Americans suffer from bone injuries (US Department of Health, 2004). As injury occurs, bone has a self-healing mechanism by removing necrotic tissues and replacing them with newly generated cells over time (Dimitriou et al., 2011; Burchardt, 1983). This mechanism allows the injured bone to recover to its pre-injured condition, but this process is extremely slow and can lead to abnormalities in terms of shape and size (Pilia et al., 2013). Moreover, there are times when this self-healing mechanism can fail due to large bone defects caused by situations such as major trauma/disease, infections, compromised blood supply, etc. (Leach and Mooney, 2004; Oryan et al., 2014). To overcome those problems, surgical procedures are essential. Bone grafting is one of the most commonly used surgical procedures for bone defects. A bone graft is a type of implant to optimize and accelerate the bone healing process, it provides a platform for newly generated cells to form on, and provides necessary mechanical supports to ensure structural stability of the defective bone (Brydone et al., 2010; Hannink, 2011). Bone grafts can be classified into three categories: autograft, allograft, and synthetic implant. Autografts are harvested from the patients, they have low rejection risk at the cost of increased patient morbidity. Allografts are harvested from a donor or animal, which are similar to the previous category in terms of mechanical properties and structural features and would not increase patient morbidity. However, there might be a possibility of rejection and disease transmission. While autografts and allografts contain limitations, synthetic implants make great alternative options. Synthetic implants have no patient morbidity, no risk of disease transmission, and, with 3D printing techniques, they are highly

customizable (Oryan et al., 2014; Kundu et al., 2014; Mironov et al., 2009). Therefore, synthetic implants are superior for bone grafting.

1.2 Literature Review

According to a study (Amini et al., 2012), every year more than 0.5 million bone grafting surgeries are carried out in the United States, and the number is increasing yearly. With such a high demand, many studies have been done in all fields related to bone grafting.

1.2.1. The Hierarchical Structure of Bone

Bone, as shown in Figure 1.2.1.1, has a complex hierarchical system. A strong outer compact layer appears at the macroscale, this compact bone is made of osteons and Haversian canals near the microscale. Inside the osteon, there are multiple arrangements of collagen fibers with collagen fibril arrays. At the nanoscale, the fibril arrays consist of a matrix of bone crystals and collagen molecules. The bone crystal, known as mineral apatite, is made of hydroxyapatite (HAp) (Nair et al., 2013).

Approximately 50% of a bone's weight is in a modified form of HAp (Junqueira et al., 2003). Stoichiometric HAp, as a form of calcium apatite, is represented by the formula $\text{Ca}_{10}(\text{PO}_4)_6(\text{OH})_2$, and it has a hexagonal crystal system, with its unit cell shown in Figure 1.2.1.1(g).

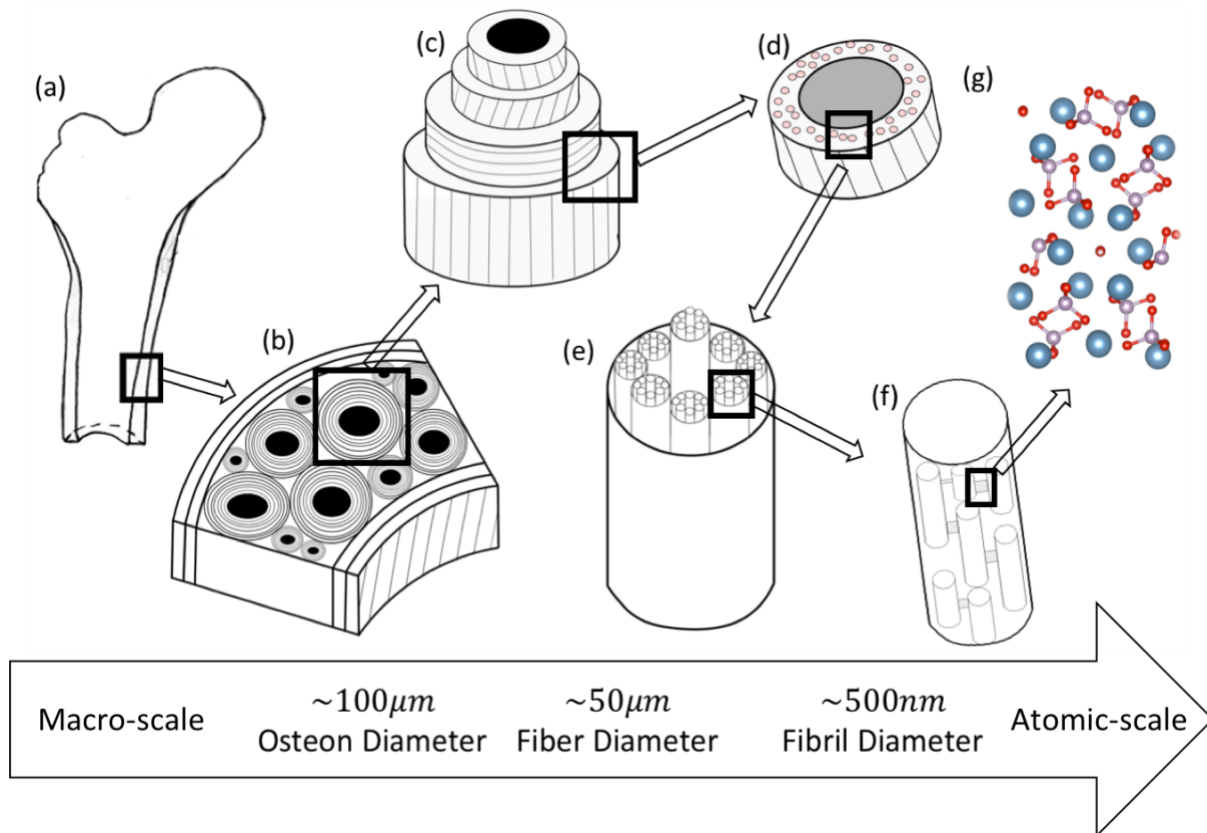


Figure 1.2.1.1: Schematic hierarchical structure of a human bone. (a) The compact femur is made of osteons and Haversian canals. (b) Inside the osteon system, there are multiple arrangements of (d) collagen fibers, which are filled with (e) collagen fibril arrays. (f) These fibril arrays consist of a matrix of bone crystals and collagen molecules. (g) The bone crystal, also known as mineral apatite, is made of HAp.

1.2.2. Background of Implants

Synthetic implants are typically in the form of scaffolds with an interconnected pore network (Kundu et al., 2014). When designing such a scaffold, several basic properties need to be considered; those include biocompatibility, biodegradability, biomechanical compatibility, and porosity and pore size. Biocompatibility is one of the most important factors. In order for cells to begin generating harmlessly, scaffolds must allow the bone cell to adhere without producing any toxicities to the host. A well-designed bone scaffold would help new blood vessels to form in a few weeks after implantation and minimize the chance of rejection or immune reaction at the same

time. Good biodegradability, as the second required property, also plays an essential role in bone grafting. Due to the fact that these implants are not designed to last permanently, biodegradable design is necessary for synthetic bone grafts. Scaffolds with this design would allow new cells to replace the synthetic scaffolds eventually. Similar to the previous property, the byproduct produced during the process of degradation should not be toxic and should be able to leave the body without interfering with other organs. Thirdly, biomechanical compatibility is also very important for synthetic bone grafts as a measurement of their properties. An ideal bone implant should have the same mechanical properties as the host, and it should be strong enough to handle mechanical stress during practices such as surgeries (Bose et al., 2012). Lastly, scaffolds should have a proper porosity and pore structure as well, to maintain sufficient nutrition and oxygen that are required for cellular proliferation. It has been shown that the minimum pore size required for scaffold structure is 25 micrometers (Maggi, 2018). A scaffold structure with high porosity is often considered a cellular solid (Gibson and Ashby, 1999). However, as the porosity and pore size increase, the mechanical strength decreases; so that in order to alleviate this negative effect and maintain the required high porosity and large pore size spontaneously, we can reduce stress concentration with some specially designed structures. Honeycomb sandwich structure (Figure 1.2.2.1) is a great example of those specially designed structures based on bio-inspiration (Gibson and Ashby, 1999). As the name suggests, in nature honeycomb structures exist in honeybees' nests. Beyond that, this structure can also be found in rocks, bones, tripe, and so on. This is a structure which could minimize the material usage and reduce structure weight while remaining relatively high out-of-plane compression properties and shear properties (Wahl et al., 2012). It is also a structure that can provide very good catalyst supports (Carty and Lednor, 1996). Engineers have adopted this structure since World War II, and it has been widely used in the aerospace industry

(Gibson and Ashby, 1999). Besides the traditional honeycomb structure, the square and triangular honeycomb structure are also being widely used for various applications (Compton and Lewis, 2014). With advances in nanotechnology, research on 3D nanolattice designs are also becoming popular; these nanolattices could be in different geometries including octahedron, Kagome, tetrakaidekahedron, and so on. Nanolattice structures are able to achieve porosities over 95% while maintaining relatively good mechanical properties (Maggi, 2018; Montemayor and Greer, 2015). However, those nanolattice structures are still under research and development, and not ready for real life applications.

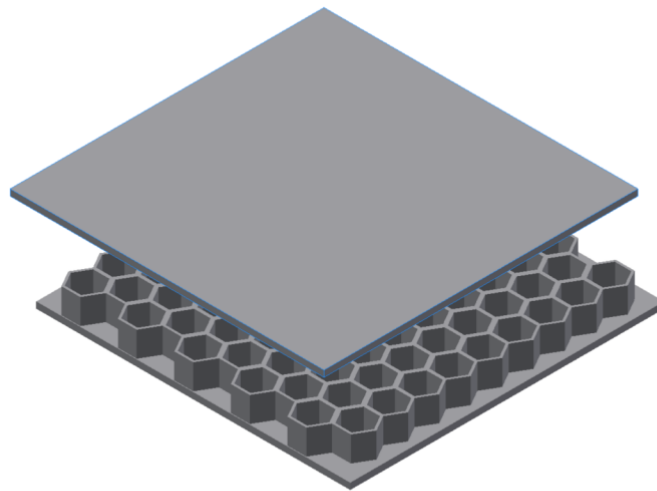


Figure 1.2.2.1: A honeycomb sandwich structure illustration. A layer of honeycomb core is in the middle of two face sheets.

In addition to those four basic properties mentioned above, the surface texture of synthetic implants is also an interesting topic to look into. As the outermost face, surface texture can define some surface properties of synthetic implants. These surface properties include protein adsorption, cell adhesion ability, and so on (Alam, 2015). From the tribological point of view, nano/micro

surface texture also could define the friction on the surface of the synthetic implant (Si et al., 2015). From a bone regeneration perspective, protein adsorption and cell adhesion ability are two important properties for surface structure. Protein adsorption can happen as soon as the implant is being inserted, cells would arrive at the surface of the implant but only interact with the adsorbed protein instead of the interface of the implant. The cell adhesion ability is the ability of the implant surface to adhere to the cells. It is a very important property; the cell growth and proliferation would be better with higher adhesion ability on the implant surface (Alam, 2015). There are multiple ways to modify the surface to control cell adhesion, to reduce protein adsorption and to reduce or increase friction on the surface. One of the most common method is to chemically modify the surface. This method usually put a layer of chemical coating on the top of the implant surface to control the protein adsorption and cell adhesion (Collier et al., 1997; Anselme et al., 2010). Besides chemistry, surface topography also plays an important role in both protein adsorption and cell adhesion. Surface roughness is one of the factors that is directly related to protein adsorption rate and cell adhesion ability (Rechendorff et al., 2006; Curtis and Wilkinson, 1997). For a scaffold that is used for bone repairing implantation purpose, it should have good protein adsorption ability and cell adhesion ability to help speed up the healing process (Alam, 2015).

Previous studies have implemented Finite Element Analysis (FEA) to optimize scaffold structures based on computer analyzed stress distribution, as fatigue cracks always initiate at the peak stress point (Schijve, 2014; Bargmann et al., 2013; Zok, 2005). FEA is a numerical method for engineering problems, especially for structural analysis (Logan, 2011). However, to manufacture scaffolds precisely based on computer-generated Computer-Aided Drawing (CAD) models is nearly impossible using conventional techniques as they do not have the flexibility to manufacture highly customized scaffolds (Huang et al., 2013). Therefore, we can adopt three-

dimensional (3D) printing technology to achieve the requirements of precision and accuracy. This advanced technique usually performs a layer-by-layer procedure and has been used to produce nanometer to meter-sized scaffolds throughout the past decade (Mueller, 2012). There are different 3D printing methods such as binder jetting, directed energy deposition, material extrusion, material jetting, powder bed fusion, sheet lamination, and vat photopolymerization (Do, 2015; Derby, 2012). Thus, in theory, we can fabricate highly customized and optimized structures by adopting this technique.

1.2.3. Materials and Substitutions

Present-day synthetic implants are mainly made out of titanium alloys or stainless steel (Andreiotelli et al., 2009), and some are made of other metallic materials. While those materials provide great strength to support the scaffold structure under different loading conditions, toxic corrosion byproducts spread throughout the patient over time (Puleo and Nanci, 1999). Besides the toxic byproducts, metallic scaffolds also have biomechanical compatibility problems. Young's modulus of metallic materials are usually over 10 times higher than trabecular bone and 2 times higher than cortical bones (Niinomi and Nakai, 2011). For example, Young's modulus of cobalt-chrome alloy is 200 GPa. However, Young's modulus of trabecular bone and cortical bone are about 1 GPa and 18 GPa, respectively (Ridzwan et al., 2007; Huiskes, 1993). The difference in Young's modulus between scaffold and bone would cause stress shielding. According to Wolff's law, bones need to remodel themselves under loadings (Frost, 1994). For this reason, when the loading on a bone decreases it would stop remodeling and become less dense. For bone grafting, this phenomenon would lead to implanted scaffolds not being able to firmly fix in the bone any more (Nagels et al., 2003). To overcome those problems, non-toxic biocompatible ceramic materials could be great alternative materials for such implants. Ceramic materials such as HAp is

often used in bone replacement because of the chemical similarity between calcium phosphates (CaPs) and bone minerals (Burchardt, 1983). It is therefore one of the most commonly used calcium phosphate bio-ceramic materials in such applications. One of the methods to reveal the true potential of ceramic materials is to estimate their mechanical properties through computational simulations such as Density Functional Theory (DFT). DFT is an *ab initio* based method to predict material elastic properties (Menendez-Proupin et al., 2011). A number of DFT studies on ceramic materials have been carried out by comparing DFT results with experimental results. Due to the nature of ceramic materials, their material properties, such as strength, could be affected by substitutions that are either intentionally engineered or naturally occurred post insertion. For instance, HAp is conducive to a number of different cationic substitutions (ions such as Mg, Zn, and Ag) and anionic substitutions (such as F, CO₃). Thus, *in vivo*, pure phased HAp that occurs naturally can rarely be found. Those cationic and anionic substitutions can significantly affect a ceramic material's physical, chemical, and biological properties (Shepherd et al., 2012). However, the effect of substitutions on mechanical properties of a scaffold at macroscale is uncertain, and it could be an interesting topic to investigate.

1.3 Thesis Overview

The present research focuses on improving the strength of scaffold structures based on bio-inspiration, replacing common metallic materials with potentially more biocompatible ceramic materials, studying the effects of substitutions, and improving surface properties with bio-inspired engineered surface textures.

The aim of this thesis is to develop a better synthetic implant design through bio-inspired designs and computational simulations. Chapter 2 focuses on the design of implant scaffolds and surface textures. Chapter 3 goes through the methods to investigate the potential of a bio-inspired

scaffold structure made out of HAp and its surface textures by using a multiscale computational method. The elastic constants of HAp are calculated by DFT at a nano-scale level. These constants are then scaled by an empirical equation based on micro-scale level porosity and are used for Finite Element Analysis (FEA) simulations. Computational models to investigate the effects of substitutions on HAp material and HAp-made scaffolds are generated and analyzed. Surface textures of the implant scaffolds are also very important, and the stress level on the surface can be affected by the geometry of textures. Therefore, the influence of cone or hemisphere surface textures on the stress level are also explored. Chapter 4 focuses on the results of this study. Based on the results, the bio-inspired scaffold has a lower stress level compared to other traditional scaffold designs, which could potentially be a better bone implant design. It is also found that substitutions not only have a major effect on the elastic constants of HAp materials but also have some effect on the stress level in the scaffolds. Considering different substitutions and endless possibilities of combinations, this could eventually lead to a new route in designing implant materials. For the surface texture study, two surface textures are compared. Those two surface textures are based on two different bio-inspired surface structures: cone surface structures and hemisphere surface structures. The focus of this study is not to verify the cell adhesion and protein absorption abilities of the newly designed textures, but rather the stress distribution and likely failure criteria. These studies include changes in maximum stress of the surface textures for different surface structure shapes, number of layers, coating thicknesses, and distances between surface structures. The study shows a number of different ways to reduce stress concentration on the surface texture, which could potentially lead to a longer-lasting scaffold surface.

CHAPTER 2: SCAFFOLD AND SURFACE TEXTURE DESIGNS

For a scaffold implant design, it is very important to design the structure of scaffolds efficiently. The structure of the scaffold is directly linked to the healing and mechanical performance of bone implants. Beyond that, a good surface design could further improve the healing performance of implants and make the surface of implants last longer. So, this chapter explores the designs of scaffolds and their surface textures.

2.1. Scaffold Designs

Bio-ceramic HAp is a material with very high strength and has been a popular material in the synthetic implant industry. The atomic configuration of HAp could be one of the reasons for its high strength. Based on its atomic configuration, some geometry patterns were discovered (Clint, 2015). From Figure 2.1.1, geometric patterns are observed on the OH-surface and Ca-surface of a HAp atomic model. Hexagonal channels are running through the HAp cells on the OH-surface, and triangular channels are also clearly crossing over the HAp cells on the Ca-surface. Triangular channels appear to be broken down by hexagonal channels due to their position and orientation; thus, all channels inside the scaffold become interconnected. Based on this geometry pattern, a bio-inspired scaffold is developed. This scaffold is called HAp inspired pores scaffold, and it has a porosity of 60% with an average pore size of 0.24 mm².

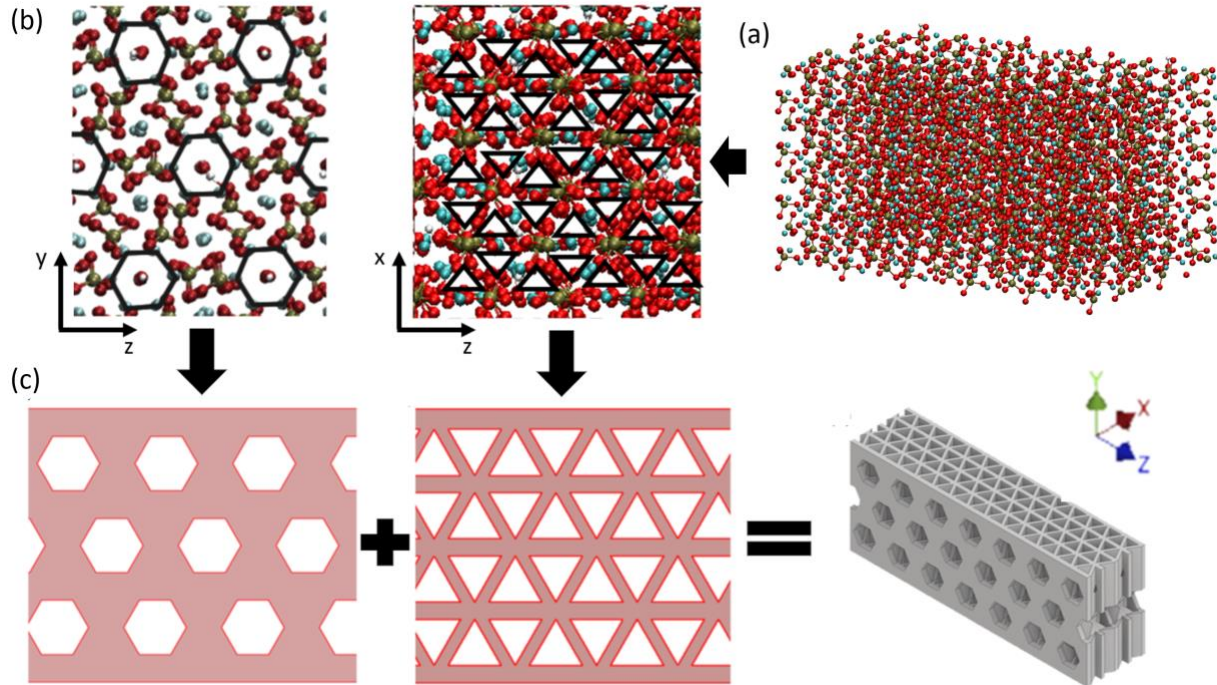


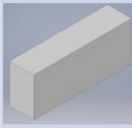


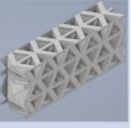
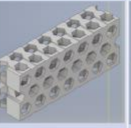
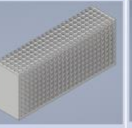
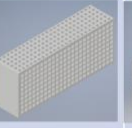

Figure 2.1.1: The atomic configuration of hydroxyapatite and the geometric design of the HAp inspired scaffold. (a) HAp atomic structure isometric view. (b) Triangular channels are shown on Ca-surface (xz -plane); hexagonal channels are shown on OH-surface (yx -plane). (c) The bio-inspired scaffold design is based on the atomic configuration of HAp. Hexagonal pore channels are on the yz -plane, and triangular pore channels are on the xz -plane.

To see if the HAp inspired pore scaffold is structurally suitable for implantation, six base scaffolds with common designs are also created for comparison. They can be categorized into three groups: large pores group, small pores group, and solid. Four base models fall under the large pores group: square pores scaffold, round pores scaffold, triangle pores scaffold, and hexagon pores scaffold. The square and the round pores are two shapes that are most commonly seen in scaffold structures; when these two models are at 60% porosity, the average pore sizes are about 0.3364 mm^2 and 0.3367 mm^2 , respectively. The triangle and the hexagon pores scaffold are designed separately such that the two shapes are mutually exclusive in each design and are used to compare to the HAp inspired pores scaffold. When the latter two models are at 60% porosity,

the average pore size is about 0.2372 mm² and 0.2831 mm², respectively. The small pores group contain a smaller pore version of the square scaffolds and a smaller pore version of the round scaffolds from the large pores group. The average pore size of the smaller pore square and round scaffolds are approximately 0.0315 mm² and 0.0314 mm², respectively, at 60% porosity. Despite previous research suggests that scaffolds with smaller pores are not suitable for bone cell regeneration (Karageorgiou and Kaplan, 2005; Polo-Corrales et al., 2014), these models function as a tool to investigate the effects of pore size on the mechanical properties of scaffolds. All scaffolds in the large pores group have 0.01 mm radius fillets for all interior corners, and all scaffolds in the small pores group have 0.002 mm radius fillets for all interior corners. The solid model in this simulation is a bulk block used as a control model, which shares the same overall size with the other models.

In order to study the geometric effects of pores, except for the solid model, all other models are set to about 60% porosity scaffolds with 60% porosity is reasonable for bone cell regeneration purpose. A series of 30% porosity models and a series of 45% porosity models for scaffolds in the large pores group are also created to explore the influence of porosity variance. These porosity levels are created by decreasing the average pore size of the models which are set to 60% porosity level. Models of the bio-inspired scaffold along with several different common scaffold designs are generated by Inventor Professional 2017 (Autodesk, Inc., USA) as shown in Table 2.1.1.

Table 2.1.1: Different models of scaffold structures, which are used in the simulations.

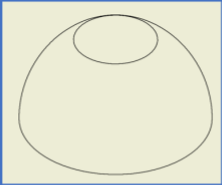
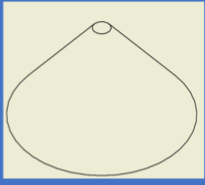
Model	Solid	Round Pores	Square Pores	Triangle Pores	Hexagon Pores	Small Round Pores	Small Square Pores	HAp Inspired Pores
Figure								
Overall Dimensions	6.277 mm (Length) X 1.543 mm (Width) X 2.509 mm (Height)							
Porosity	0%	~ 30%, ~ 45%, ~ 60%	~ 30%, ~ 45%, ~ 60%	~ 30%, ~ 45%, ~ 60%	~ 30%, ~ 45%, ~ 60%	~ 60%	~ 60%	~ 60%
Weight (g)	0.077	0.055, 0.041, 0.030	0.055, 0.042, 0.031	0.055, 0.041, 0.032	0.055, 0.040, 0.030	0.030	0.031	0.031
Total Surface Area (mm ²)	58.6	108.2, 108.2, 103.0	114.1, 113.4, 106.9	144.9, 142.4, 135.3	115.1, 112.9, 108.1	265.1	284.2	243.0
Volume (mm ³)	24.31	17.55 , 12.84, 9.65	17.51, 12.85, 9.78	16.89, 11.93, 9.28	16.27, 11.35, 8.68	9.39	9.67	9.69

2.2 Surface Texture Designs

The surface texture is an external boundary and the outmost layer of a structure, and they are crucial for bio-materials and synthetic implants. A good surface texture design for implants should be able to enhance the cell adhesion and protein absorption ability of the implanted scaffold. The surface texture is made up of surface structures. Different surface structures can be used to create surface textures. Previous studies used micro-pillar structures on the surface to help cell growth (Yang, 2006), and used nanopyramid structures on the surface to modify surface roughness and to enhance the protein absorption (Muller et al., 2001). However, both pyramid and pillar structures contain pointing and sharp edges, which are geometrically good for stress concentration when the surface structure is under force or pressure. Although the designs of surface structures of implant scaffolds are not intended to be put directly under loadings, bearing some levels of loadings is unavoidable. Therefore, it is necessary to find a way to reduce stress concentration on those surface structures to make the surface texture last longer. Crabs have a strong exoskeleton,

and their chela is even more incredible; they can use the chela to crack open shellfish, like clams (Weis, 2012). When we look closer to the inner edge of their chela, some serrated structures can be seen. Based on those structures, two bio-inspired surface structures are designed as shown in Table 2.2.1. One is a hemisphere structure, and the other is a cone structure. Both surface structures are $3\ \mu\text{m}$ in depth with $3\ \mu\text{m}$ radius bottom.

Table 2.2.1: Surface structures for surface texture simulations. Two base structures are hemisphere and cone.

Model		
Name	Smooth Hemisphere Surface Structure	Smooth Cone Surface Structure
Overall Dimensions (mm)	$0.006 \times 0.006 \times 0.003$	

CHAPTER 3: MULTISCALE MODELING METHOD

This study uses a multiscale approach that obtains the elastic constants of HAp from DFT calculations, which are then scaled by empirical relations based on the porosity of scaffolds. The scaled elastic constants serve as the input for the corresponding scaffold in FEA simulations, including compressive and bending loading cases.

3.1. Elastic Constants of Stoichiometric HAp

HAp, as a synthetic material, can be prepared using various methods (Inzana et al., 2014; Du et al., 2015). The synthetic HAp is usually in the form of powder and can be used as a material for 3D printing using the binder jetting method. Binder jetting is a 3D printing process in which “a liquid bonding agent is selectively deposited to join powder materials” (Eshraghi, 2015). Previous studies have reported the fabrication of HAp scaffold structure with HAp powder and power binders by using additive manufacturing techniques. However, the mechanical properties of scaffolds produced by different combinations of printing tools and HAp powder binders can critically vary (Cox et al., 2015; Zhou et al., 2014). For example, according to Cox et al. (2015), the yield stress of their 3D printed 55% porosity HAp scaffolds vary from 0.10 MPa to 0.78 MPa. Therefore, in this study, the theoretical mechanical properties of stoichiometric HAp based on DFT calculations at the atomic level are used. The DFT calculation results of elastic constants are shown in Table 4.3.4 (Deymier et al., 2017). The DFT calculations predict changes in surface energy and elastic moduli. HAp material has been considered as an isotropic material in previous research (Ren et al., 2009); in contrast, the microscopic behavior of HAp appears anisotropic (Ching et al., 2009). Due to the symmetric feature of hexagonal crystal structure, HAp can be considered as a transversely isotropic material (Deymier et al., 2017).

3.2. Substitution Effects on the Elastic Constants of HAp

Substitution is a factor needed to be considered when using HAp as the material for implants. Previous research (Shepherd et al., 2012) has shown that even a small amount of substitutions would have significant effects on solubility, osteoclastic response, thermal stability, and osteoblastic response. In vivo, it also significantly affects degradation and bone regeneration (Shepherd et al., 2012). Both cationic and anionic substitutions could happen on the bio-ceramic scaffolds after insertion. This study investigates the effects of three common substitutions on HAp: Zn, Mg, and carbonate substitutions. The effects of cationic substitutions, such as Zn and Mg, on the elastic constants of HAp are investigated by Aryal et al. (2015) through DFT calculation. They used Mg and Zn atoms to replace Ca atoms inside HAp unit cell. With different numbers of Ca atoms being replaced, HAp unit cells with different volume percentage from 0%-25% of Mg or Zn substitution are created.

Deymier et al. (2017) investigated the effects of carbonate substitutions on HAp. As shown in Table 4.3.4, they created apatite lattice models of B-type carbonate substitution for phosphate groups in the HAp and calculated their elastic constants. The weight percentage of substitution is 6.3% and 13.4%.

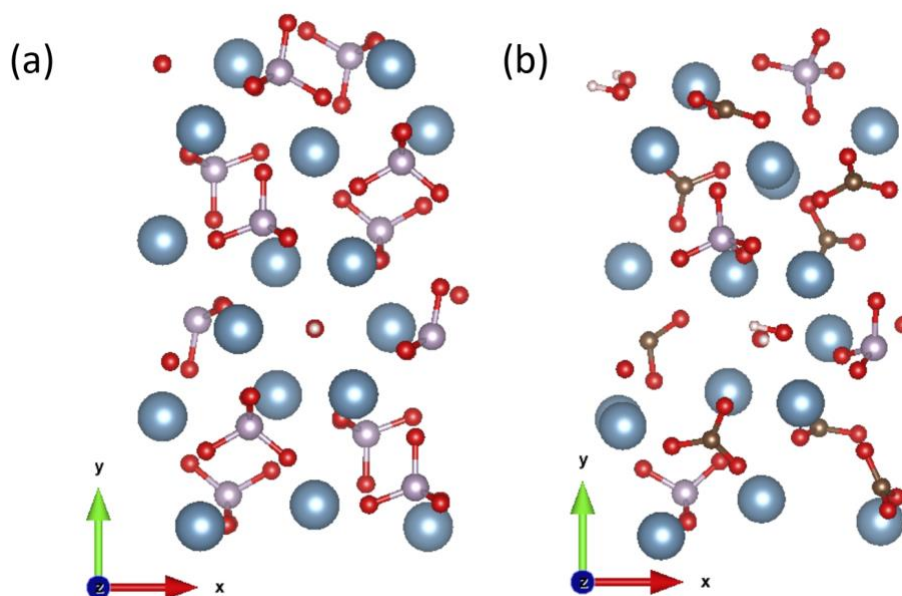


Figure 3.2.1: Illustration of B-type carbonate substitution (brown and red atom group) for phosphate groups (violet and red atom group) in the HAp model. Calcium, phosphorus, carbon, hydrogen, and oxygen atoms are shown in blue, violet, brown, white, and red, respectively. Apatite lattice models shown here are used for DFT calculations. (a) 0 wt% carbonate substitution, (b) 22 wt% carbonate substitution.

We want to further explore the effects of higher carbonate substitutions on HAp. In this study, a lattice model of B-type carbonate substitution for phosphate groups of HAp at 22 wt% is created as shown in Figure 3.2.1. An orthorhombic unit cell with 88 atoms is used to simulate stoichiometric HAp. The initial lattice parameters are based on experimental measurements, those values are: $a = 9.424 \text{ \AA}$, $b = 16.322 \text{ \AA}$, $c = 6.879 \text{ \AA}$, $\alpha = \beta = \gamma = 90^\circ$ (Hughes et al., 1989). A rectangular prism is formed by the unit cell replicated in all three dimensions. The initial dimension is $a \times b \times c$. To calculate elastic constants of 22 wt% carbonated HAp, a substituted HAp model is created. To create this model, four Ca atoms are removed and eight (PO₄) are replaced by (CO₃). Each carbonate ion is at least 4.5 \AA apart from each other. The locations of carbonate substitutions are chosen to match previous studies to minimize the total energy of the system (Astala and Stott, 2005; Deymier et al., 2017). DFT is used to calculate the elastic constants of the substituted HAp,

with the Quantum ESPRESSO package (Giannozzi et al., 2009) being used for DFT calculations. For plane-wave basis sets, the energy cut off is set to 60 Ry, and for the charge density, the cut off energy used is 360 Ry. During the DFT calculation, the unit cell is strained in different directions to calculate various elastic constants. Energy convergence for bulk calculations is observed at a $2 \times 1 \times 2$ k -point grid. For energy convergence, the difference in energy between two consecutive steps must be less than 10^{-6} Ry. Regarding forces, the convergence must be less than 10^{-3} Ry/Bohr (Deymier et al., 2017). Empirical relationships between energy and strains are evaluated, and the elastic constants are determined by fitting the energy curves (Menendez-Proupin et al., 2011).

3.3. Elastic Constants Scaling

FEA can predict the influence of the geometric features of scaffolds, but it does not provide any significant variation in the results of porosity effects. Therefore, for porosity dependence, it requires an appropriate material model. A previous study reported the porosity dependence in HAp with an empirical relationship based on experiments (Ren et al., 2009). This study adopts an empirical relationship of the HAp to model the porosity dependence. The empirical relationships (Equations 3.3.1 and 3.3.2) of Young's modulus (E) and shear modulus (G) are an exponential function porosity (p). The porosity dependence is considered in the model by considering Young's modulus and shear modulus dependence in the compliance matrix (C) using the following equations:

$$E = E_0 \exp(-b_E p) \quad (3.3.1)$$

$$G = G_0 \exp(-b_G p) \quad (3.3.2)$$

where E_0 , G_0 , b_E , b_G and p are the Young's modulus, shear modulus of stoichiometric HAp, exponential constant for Young's modulus, shear modulus, and porosity respectively. The

exponential constants for Young's ($b_E = 3.4$) and shear modulus ($b_G = 3.54$) are evaluated by fitting the experimental results from the previous study (Ren et al., 2009).

3.4. FEA Simulation Setups for Computational Models Developed

The numerical study uses FEA with the commercially available software Workbench (ANSYS® 17.2). As shown in Table 2.1.1, all 16 scaffold models and 12 surface texture models are created by Autodesk Inventor Professional 2017 (Autodesk, 2017) and exported to ANSYS Workbench for FEA simulations.

3.4.1. Scaffold Simulation

3.4.1.1. With Stoichiometric HAp Material Property

Three loading cases are created to simulate three loading cases that bone grafts could experience (Figure 3.4.1.1.1): uniaxial compression case, biaxial compression case, and bending case (Table 3.4.1.1.1). The boundary conditions are defined in Figure 3.4.1.1.2. One side of each scaffold is fixed in the uniaxial loading case, and a distributed load is applied (150 N) to the surface on the opposite side of the fixed surface; other surfaces are assumed to be free surfaces. The boundary conditions are similar in the biaxial loading case, except for another distributed load that is applied to the surface on the positive x -direction side of scaffolds, and the surface on the negative x -direction is also fixed. For the bending simulation, two supporting points are fixed; the indenter at the top is applying a 30 N force towards the negative y -direction. The magnitude of the force is selected based on the yield stress of the HAp material, as literature has reported the stress-strain curve for different directions in HAp material (Ching et al., 2009). This study tries to limit the stress during the simulation within the linear elastic region since it is focusing on optimizing the scaffold design by modifying pore shape and arrangement. All scaffold models are numerically simulated using these three loading cases. All scaffold models are meshed with tetrahedral

quadratic elements. A convergence study is performed to guarantee the mesh quality in each model by converging the stress and strain to less than 5% difference.

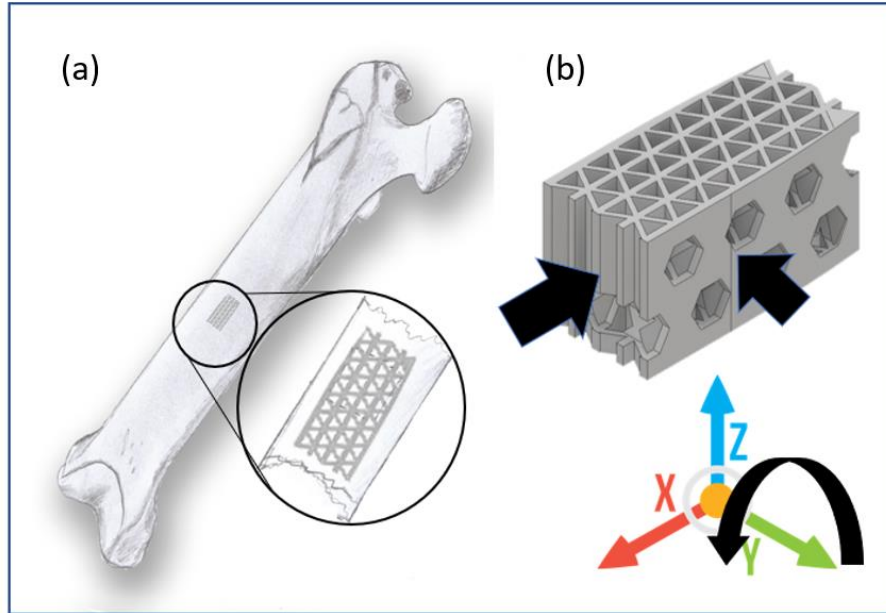


Figure 3.4.1.1.1: The implant is under complex loadings after (a) insertion. Such loadings including compressive forces from different directions, bending, and so on. (b) In this study, loading conditions such as compressive forces from x and y -direction and bending in the y -direction are studied.

The distributed loadings are calculated using the following formula:

$$\sigma_a(MPa) = \frac{F(N)}{S(m^2)} \quad (3.4.1.1.1)$$

where σ is applied distributed load, F is the normal force in the specified direction, and S is the area of the loading surface.

Table 3.4.1.1.1: Applied loading value in a simulation for different loading cases.

Loading Case	x-direction (N)	y-direction (N)	z-direction(N)
Uniaxial Compression	0	0	150
Biaxial Compression	150	150	0
Bending	0	30	0

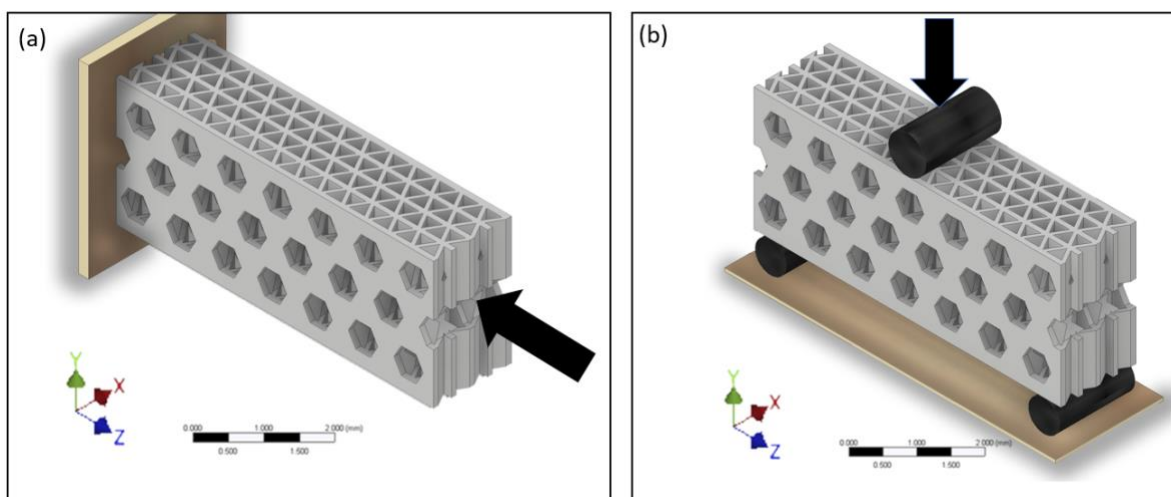


Figure 3.4.1.1.2: (a) For each uniaxial compressive simulation, a 150 N force is applied to the model towards negative z-direction. The opposed side of the force applying side is fixed. For each biaxial compressive simulation, a 150 N force is applied to the model towards negative z-direction, another 150 N force is applied to the model towards negative x-direction. The opposed side of the force applying side is fixed. (b) For each bending simulation, two supporting points are fixed. The inductor on the top is going toward to the negative y-direction with a 30 N force.

The effect of substitutions on elastic constants of the HAp material will directly affect the performance of scaffolds. To investigate the effect of substitutions on scaffolds, a series of FEA simulations are performed. The HAp inspired scaffold is used per the substitution effects study. Nine simulations are conducted, which include: 6 wt% CO₃, 13 wt% CO₃, 22 wt% CO₃, 5 vol% Zn-doped, 12 vol% Zn-doped, 22 vol% Zn-doped, 5 vol% Mg-doped, 12 vol% Mg-doped, and 22 vol% Mg-doped substitutions. In each simulation, the corresponding scaled elastic constants from

DFT calculations are applied to the HAp inspired scaffold as material properties. The uniaxial compression loading case (Table 3.4.1.2.1) is used for each simulation.

3.4.2. Surface Texture Simulation

Since the cell adhesion and protein adsorption abilities of a scaffold could be optimized by employing an engineered surface texture, it is important to have a surface structure design that can make the surface texture last longer before failure. In the surface texture study, CAD models of surface textures for simulations are created based on experiments performed by Dr. Zou's tribology laboratory (Department of Mechanical Engineering, University of Arkansas). The simulation is based on the experimental setup parameters including surface structure dimensions and the magnitude of the force applied to the top of surfaces.

In the experiments, all surface structures are set to the same size to simplify the manufacturing procedure. Surface structures are 10 μm away from each other (center to center distance) on a 5 μm thick base. Cone surface has only cone surface structures on the surface, hemisphere surface has only hemisphere surface structures on the surface. To fabricate the designed surface textures, all surface structures are fabricated via two-photon lithography (TPL) direct laser writing (DWL) with IP-Dip (Nanoscribe GmbH), and then the IP-Dip surface structures are coated with alumina via atomic layer deposition (ALD). 3D printed surface structures have layer-by-layer features, as shown in Figure 3.4.1.2.1 (e), due to the nature of additive manufacturing techniques. For the 10-layer and 20-layer versions of both cone and hemisphere surface structures, each layer is 0.3 μm and 0.6 μm thick, respectively. From scratching experiments, coefficients of friction for cone and hemisphere surface are 0.17 and 0.23, respectively. The coefficients of friction are then used in the simulation. All simulation cases are shown in Table 3.4.1.2.1. Case 1 is used to study how the maximum stress on two surface textures

change over different coating thickness, simulations in the case 2 are used to investigate the effect of distance between surface structures on the maximum stress on the two surface textures, and case 3 is used to study the effect of the number of layers on the maximum stress on the two surface textures.

Table 3.4.1.2.1: All simulation cases in the surface texture study

Case #	Surface Structures	Coating Thickness (mm)	Distance Between Structures (μm)	# of Layers
1	Hemisphere, Cone	100	10	10
	Hemisphere, Cone	200	10	10
	Hemisphere, Cone	300	10	10
2	Hemisphere, Cone	200	10	10
	Hemisphere, Cone	200	15	10
3	Hemisphere, Cone	200	10	10
	Hemisphere, Cone	200	10	20
	Smooth hemisphere, smooth cone	200	10	(N/A)

All simulations are performed using a similar setup as the 10-layer hemisphere surface simulation as shown in Figure 3.4.1.2.2. Each CAD model contains an IP-Dip base, with an alumina coating bonded to the top of the base. A counter face made of silicon is set to touch on the top of the surface structures. For cone surface, the surface structures are changed from hemisphere surface structures to cone ones. The space between each surface structure and coating thickness is also be adjusted according to the simulation requirement. During all simulations, the counter face applies a 120 μN force onto the surface structures while moving towards the negative z -direction.

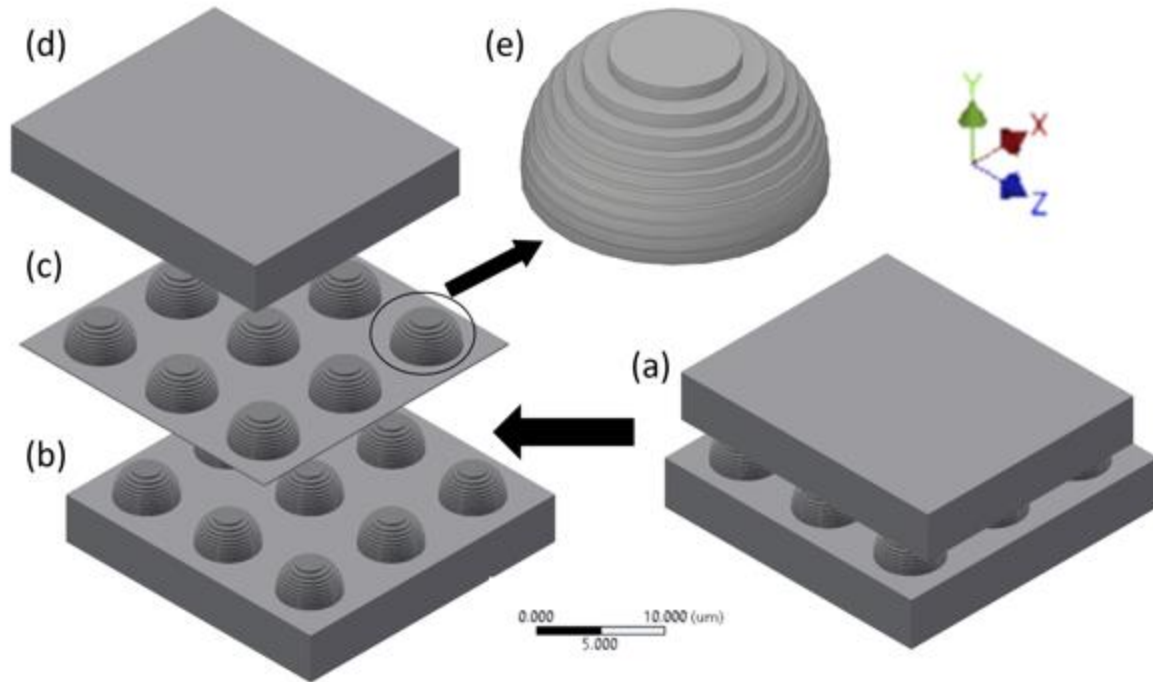


Figure 3.4.1.2.1: Example of surface texture simulation, CAD model setup. (a) The entire model consists three parts, those are (b) IP-Dip base, (c) alumina coating, and (d) silicon counterface. The (e) 10-layer hemisphere surface structures are arranged on the surface in a rectangular pattern. The distance between each surface structure is equal. During the simulations, the counter face would move towards negative x -direction.

Table 3.4.1.2.2: The material properties of materials used in surface texture simulations. ([1] Zhang et al., 2012; [2] Lemma et al., 2017)

	Al_2O_3	IP-Dip	Silicon
E (GPa)	127.9	2.75	150
ν	0.24 [1]	0.5 [2]	0.17
Hardness (GPa)	8.72	0.375	(N/A)
Yield Stress (GPa)	2.906	0.125	(N/A)

CHAPTER 4: RESULTS AND DISCUSSION

In this chapter, the FEA results for computational models of scaffolds, substitution effects, and FEA results of surface texture simulations are listed and discussed.

4.1. FEA Results for Computational Models of Scaffolds

The primary focus of this study is to compare the stress level in each scaffold structure. Thus, the normal stress along each direction is calculated for each of the different cases. To find the effects of porosity and scaffold structure on stress levels, a series of comparisons of results are performed. To compare results, the maximum normal stress along the loading direction is selected for the uniaxial compression cases. Due to the complexity of loading cases and scaffold structures, the maximum normal stress along z -axis is used for comparison in the biaxial compression cases and the bending cases.

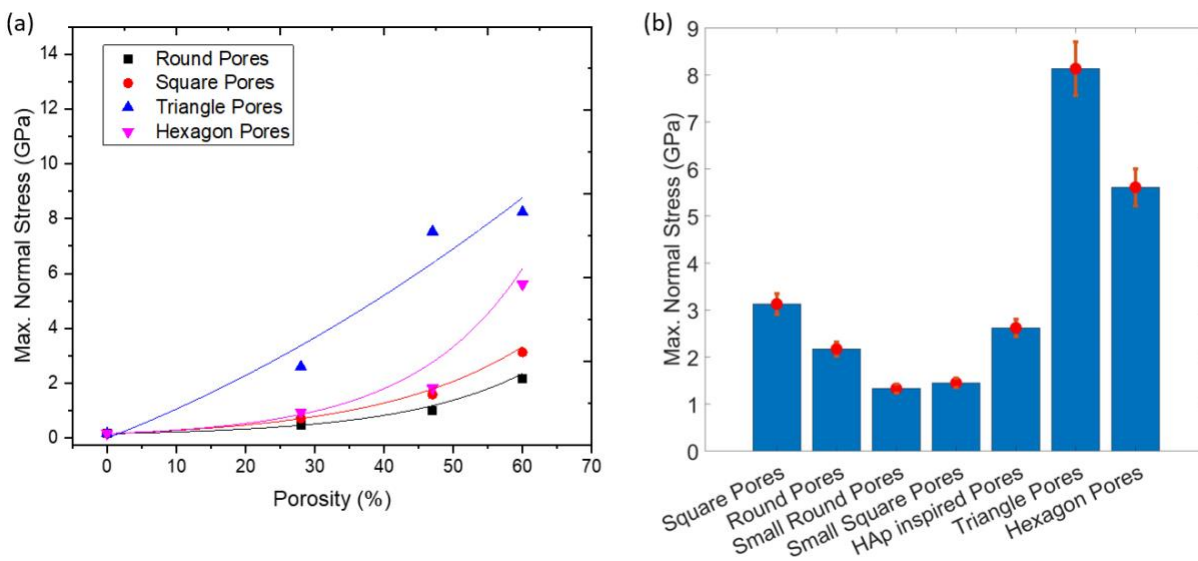


Figure 4.1.1: Uniaxial compressive simulation results. (a) Plot of max. normal stress in the loading direction of round, square, triangle, and hexagonal pores scaffolds vs. porosity. All scaffolds are under higher maximum normal stress when the porosity is higher, especially the triangle pores scaffold. (b) The max. normal stress along the loading direction of each 60% porosity scaffold. Scaffolds with smaller average pore size are under lower maximum normal stress compare to scaffolds with larger average pore size.

In Figure 4.1.1 (a), the effect of scaffolds' porosity on their stress level is studied. Maximum stress values are plotted and compared. As shown in the figure, all scaffolds in the large pores group with different porosity are simulated under a 150N uniaxial compression force, and it shows that the maximum stress along the loading directions of all four scaffolds increase when porosity is increasing. The results clearly show that, regardless of shape and arrangements of pores, all models are more likely to fail under loadings with higher porosity. This is consistent with previous research (Liu, 1997; Ren et al., 2009). However, pore shape and arrangement still play a critical role in the effects of stress levels. The maximum normal stress along the loading direction of the triangle pores scaffold increases much faster than any other models as porosity increases. This result indicates that with proper pore shape and pores arrangement, it is possible to minimize the negative effects resulting from high porosity.

To further investigate the effects of pore shape and arrangement on stress levels, scaffolds with similar porosity but different pore shape and arrangements are plotted and compared based on their maximum normal stress along the loading direction in Figure 4.1.1 (b). As shown in this figure, histograms are established to show the maximum stress levels of all scaffolds with 60% porosity that are tested under 150N uniaxial force. Both small round pores scaffold and small square pores scaffold in the small pores group have a smaller maximum normal stress than other scaffolds. HAp inspired scaffold, round pores scaffold, and square pores scaffold also demonstrate a relatively low stress level. Round pores scaffold in particular shows a lower stress level than other pore shapes with similar pore sizes. These results indicate that the shape of pores does influence stress levels.

We have also found that pore size appears to correlate with the total surface area of scaffolds. Among all scaffolds with 60% porosity shown in Figure 4.1.2, scaffolds from small

pores groups apparently have larger total surface areas compared to the large pores group scaffolds. Bone grafts with larger surface areas have been shown to perform better in bone cell regeneration (Moreno et al., 2016), and large pore size is also required for cell regeneration purpose. Therefore, although scaffolds in the small pores group have larger surface area and perform better in the uniaxial compression test, they may not be suitable to employ in applications like bone grafting due to the limited pore size. In contrast, the HAp inspired scaffold not only has a relatively large pore size and a large total surface area, but also has a lower stress level in the uniaxial compression test compared to other scaffolds, making it a potentially favorable candidate for bone grafting.

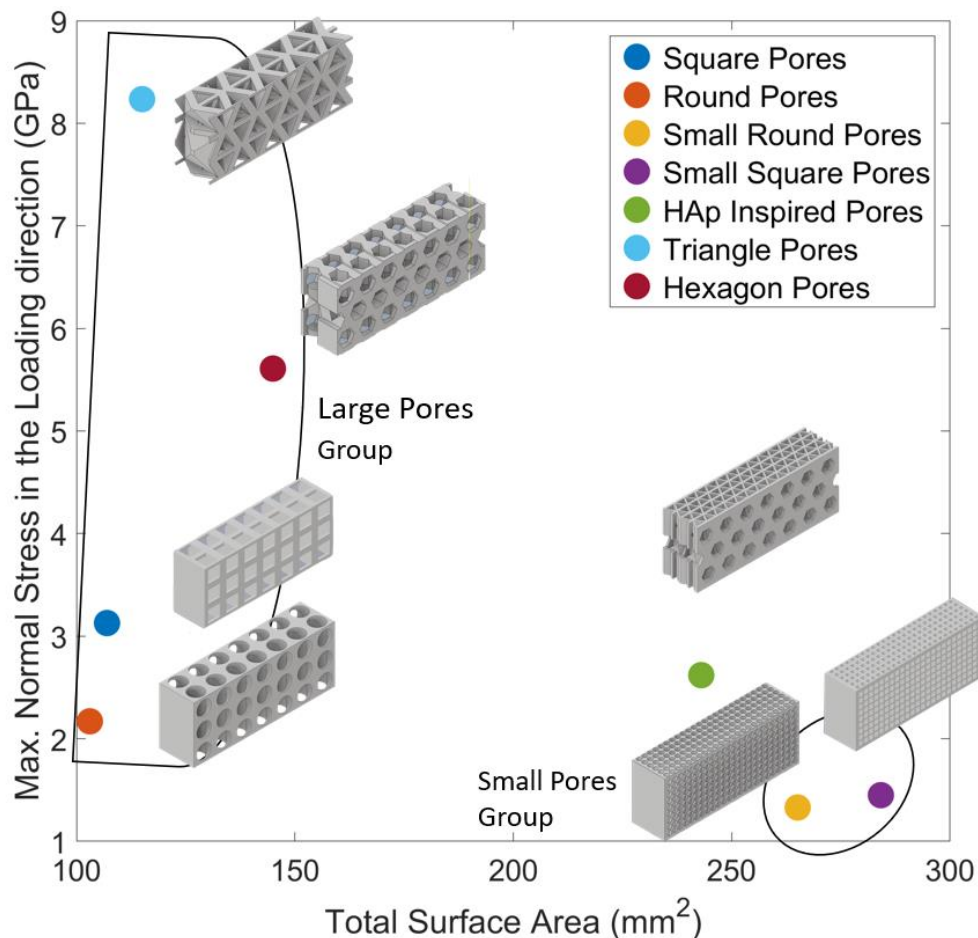


Figure 4.1.2: The relationship between maximum normal stress and total surface area for each scaffold. Based on the pore size and pore pattern, all 60% porosity scaffolds fall into 3 groups, HAp inspired pores group, large pores group and small pores group. Scaffolds with larger total surface area tend to have lower maximum normal stress in the uniaxial compressive simulations.

Biaxial compression tests and bending tests are conducted to explore the performance of scaffolds under more complicated loading conditions. Only large pores scaffolds are tested since small pores are not preferred for bone cell regenerations (Murphy, 2009). Histograms are established to show peak normal stress in both the biaxial compression test and the bending test of large pores group scaffolds and HAp inspired scaffolds, all of which are set to 60% porosity as shown in Figure 4.1.3. In the analysis, both square pores and round pores scaffolds show relatively low maximum normal stress in the biaxial compression test, but much higher maximum stress in the bending test when compared to other scaffolds. Triangle pores and hexagon pores scaffolds both show higher maximum normal stress in the biaxial compression test, especially for the triangle pores scaffold, its maximum stress reach to approximately 8.5 GPa, which is more than two times higher than the square pores and round pored scaffolds. However, in bending tests, triangle pores and hexagon pores scaffolds have significantly lower maximum normal stresses than square pores and round pores scaffolds, which are only about 2.79 GPa and 3.95 GPa, respectively. HAp inspired scaffold, on the other hand, shows the lowest stress level among all scaffolds in both biaxial compression and bending tests, which are approximately 1.78 GPa and 1.24 GPa, respectively.

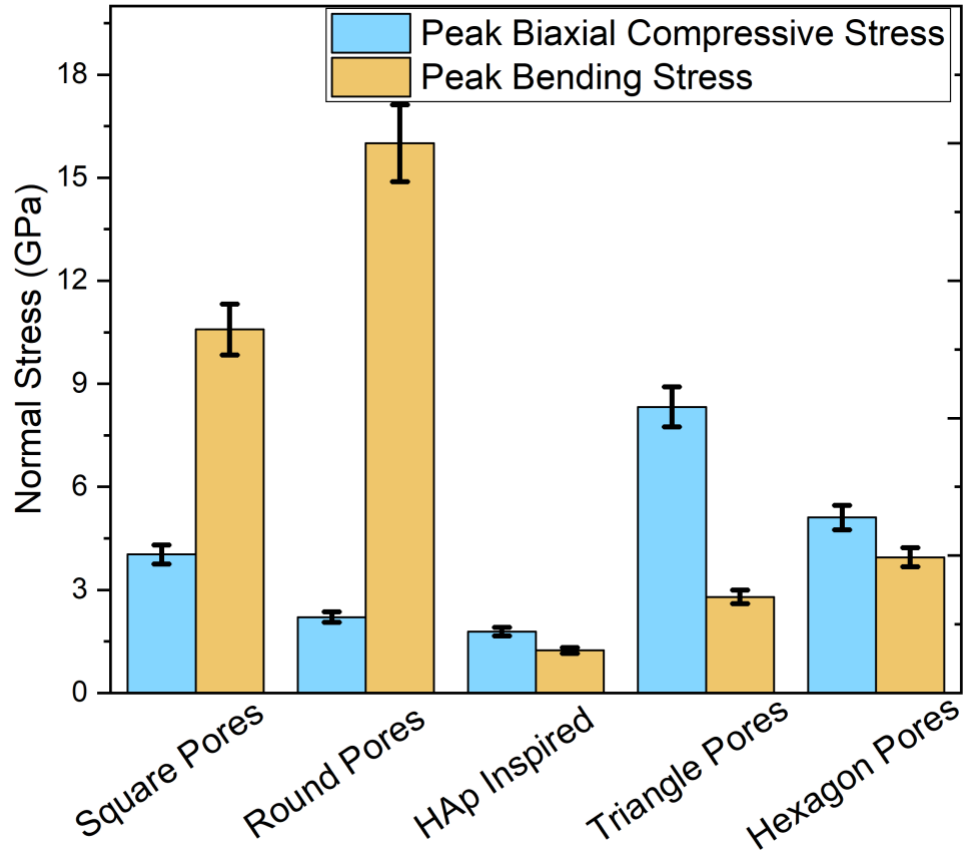


Figure 4.1.3: Biaxial compressive test and bending test results of selected 60% porosity models. The HAp inspired scaffold has lowest stress level in both biaxial compression test and bending test. Square pores and round pores scaffolds both show similar maximum normal stress in both compression and bending tests. Triangle pores and hexagon pores scaffolds both have higher maximum normal stress in biaxial compression tests, but significantly lower peak bending stress compare to the square and round pores scaffolds.

Round pores and square pores scaffolds are two of the most commonly seen scaffold structures for bone grafting (Cox et al., 2015; Murphy, 2009; Zhou et al., 2014). Both show relatively low normal stress in the uniaxial loading in comparison with other scaffolds with similar porosity under the same loading conditions. Except scaffolds in the small pores group, the round pores scaffold and HAp inspired scaffold both show a lower maximum normal stress, not only in uniaxial, but also in biaxial loading cases. On the other hand, while the square pores scaffolds perform well in the uniaxial loading case, the maximum stress in biaxial loading case is almost

two times higher than both round pores and HAp inspired scaffolds. Gibson et al. (1999) suggest that square shaped scaffolds would be under higher stress using 2D geometric analysis if the force is applied along the diagonal direction; apparently, the 3D square pore scaffold inherited this characteristic from its 2D geometry. The results of biaxial compression tests are shown in Figure 4.1.4 (a). The figure indicates that the maximum normal stress of all scaffolds appears in the z -direction, yet the overall stress level in the HAp inspired scaffolds is much lower than the square pores scaffold due to the built-in honeycomb structure. Furthermore, round pores scaffold appears to have the lowest maximum normal stress in the uniaxial compression cases, but it is not the lowest one in biaxial compression cases. All scaffolds have the maximum normal stress in the z -direction in the bending test as well. In Figure 4.1.4 (b), the maximum normal stress in the HAp inspired scaffold is also much lower than the round and square pores scaffolds. The locations where the maximum normal stress occur are located on the top middle of all three scaffolds. Due to the large pore size of the round and the square pores scaffolds, large void areas are created. When a force is applied to the area near a large void, there will not be enough support for it; as a result, large deformations appears, leading to a much higher stress level than the HAp inspired scaffold under the same loading condition. Hence, the HAp inspired scaffold appears to have a better performance under complex loading conditions among all other scaffold structures.

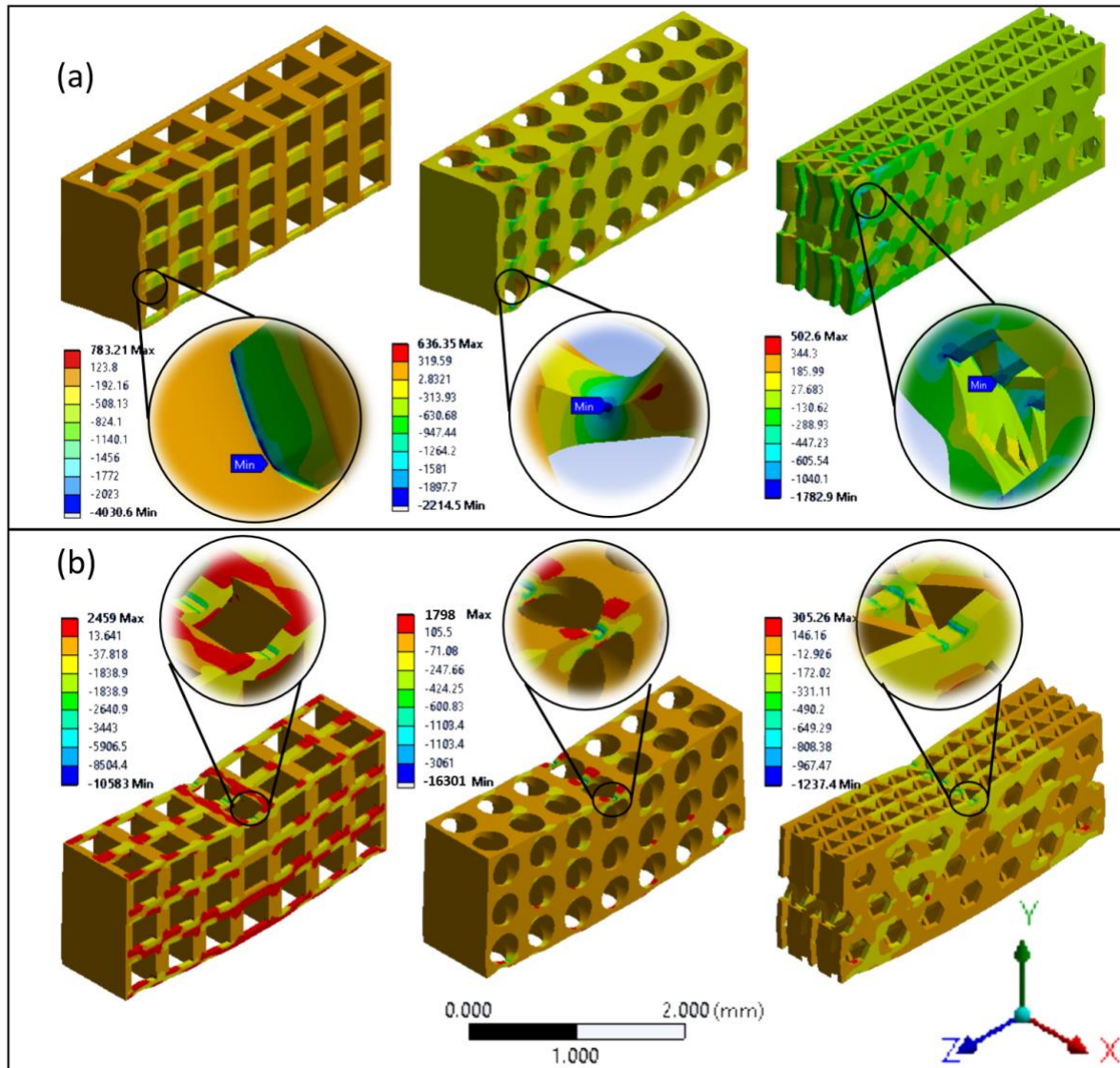


Figure 4.1.4: The normal stress distribution (unit: MPa) of square pores, round pores, and HAp inspired scaffolds during biaxial loading and bending tests along the z-direction. (a)The normal stress distribution during biaxial loading tests. (b) The normal stress distribution during bending tests. The maximum stress in each case is also stating in Figure 4.1.3.

The HAp inspired scaffold structure can be broken down into two parts as indicated in Figure 4.1.5: the large pore layer, and the truss layer. The large pore layer has large-sized pores in it, which is designed to help bone cell regeneration; it also leads to stress concentration reduction by providing hexagon shaped pore design. As the loading condition becomes complex, hexagon

pore design, unlike the square pore design, reduce the length of the center beam while remaining similar pore size to the square pores scaffolds. The truss layer provides support for loadings from the x and the z -direction using a honeycomb-like truss sandwich structure; improve the strength of the whole structure. For instance, the truss layer in Figure 4.1.5 is under 20 N uniaxial tensile force along the z -direction, and the stress distribution is very uniform. Additionally, this layer provides a large surface area to benefit bone cell regeneration due to its triangular honeycomb truss structure.

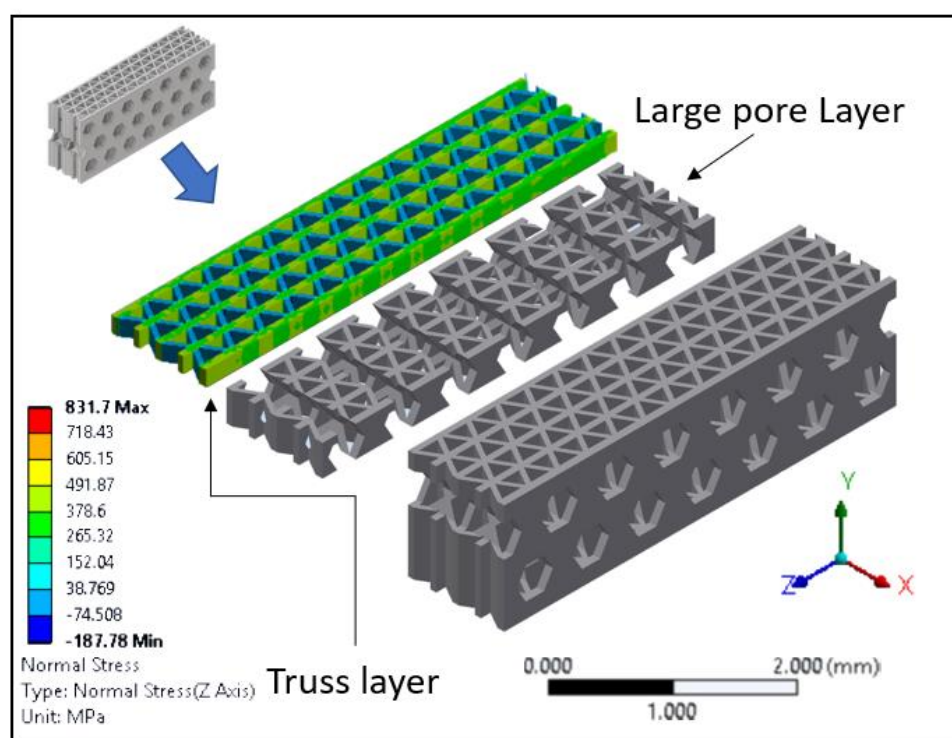


Figure 4.1.5: HAP inspired structure breakdown. The structure is made of large pores layers and truss layers. The truss layer uses a honeycomb-like truss sandwich structure to make stress distribution on the structure more uniform. The large pore layer provides large sized pores to the scaffold, which theoretically helps bone cell regeneration. This layer also provides support for stress concentration reduction by using the hexagon pore shape design.

The HAP inspired scaffold is shown to have better performance in terms of stress concentration reduction compared to other scaffold structures under the same complex loading conditions, however, there is still room for improvement. From reviewing all results, square pores

and round pores scaffolds are both found to have lower stress levels compared to hexagon pores scaffolds in both uniaxial and biaxial compression tests. While pore shapes may play a major role, pore arrangement might also be causing this. Both square and round pores scaffolds are found with an in-line pore arrangement, whereas the hexagon pores scaffolds have a staggered pore arrangement. To verify this assumption, the pores in the HAp inspired scaffold are rearranged from staggered to an in-line arrangement; the same tests are then conducted. Although the bending test results are shown in Figure 4.1.6, HAp inspired scaffold has a lower stress level after modification in the uniaxial compression test; the maximum normal stress in the loading direction in uniaxial compression test and bending test are reduced by approximately 16.2% and 6.9%, respectively. Nevertheless, the maximum normal stress of the modified version of the scaffold in the biaxial test is increased by approximately 15.9%. It is therefore clear that pore arrangement can also impact the mechanical strength of scaffold structures.

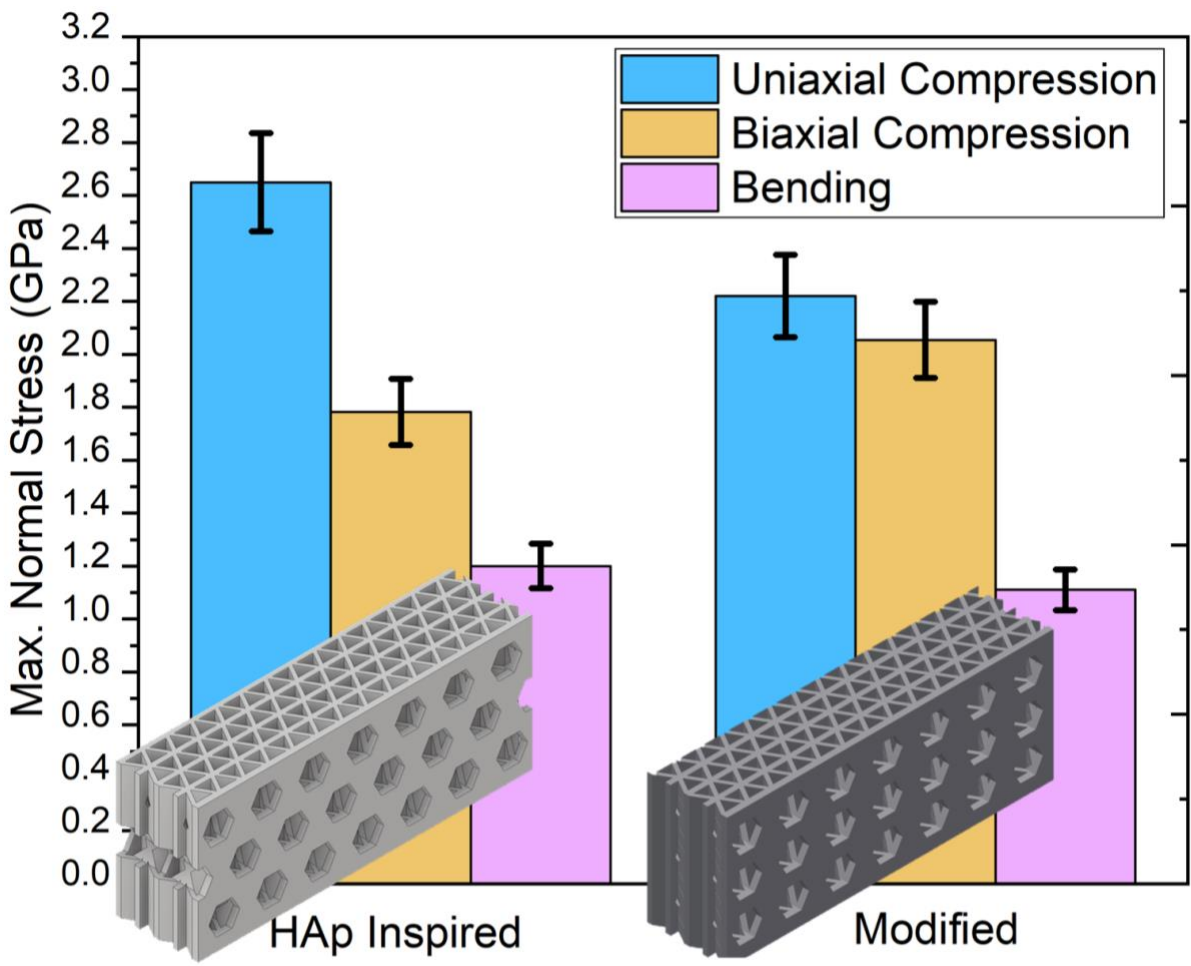


Figure 4.1.6: Comparison between HAp inspired model and modified HAp inspired model. Both scaffolds are having similar maximum stress in the bending test. The modified model has lower stress level in the uniaxial compression test but higher stress level in the biaxial test compared to the original model under the same loading conditions.

4.2. Substitution Effects

Table 4.2.1: DFT calculation results of stoichiometric HAp, carbonated HAp, Zn-doped HAp, and Mg-doped HAp. ([1] Deymier et al., 2017; [2] Aryal et al., 2015)

Unit: GPa	C11	C33	C44	C12	C13
Pure HAp ^[1]	118.58	166.38	40.4	32.27	65.73
6 wt% CO ₃ ^[1]	117.63	148.18	28.49	49.28	47.39
13 wt% CO ₃ ^[1]	118.21	128.02	24.26	29.95	45.5
22 wt% CO ₃	79.85	77.21	4.42	29.80	15.87
5 vol% Zn ^[2]	125.07	154.41	41.56	37.99	61.52
12 vol% Zn ^[2]	124.58	137.46	40.80	39.63	57.79
22 vol% Zn ^[2]	123.72	134.26	39.42	41.96	58.32
5 vol% Mg ^[2]	126.51	161.99	42.77	36.70	64.63
12 vol% Mg ^[2]	128.72	160.23	43.30	38.35	64.69
22 vol% Mg ^[2]	130.02	161.51	43.78	40.57	64.80

This study assumes that all scaffold structures are made with stoichiometric HAp, yet the crystal structure of HAp is conducive to a variety of anionic and cationic substitutions. Previous research suggests that even minor substitutions can alter the microstructure, and the crystallinity of the HAp structure in a scaffold (Supova, 2015; Shepherd, et al., 2012), so that the mechanical strength of the scaffold would be changed after being implanted. Even a bone grafting scaffold which are made of stoichiometric HAp could, later on, transform into a non-stoichiometric HAp scaffold with a possible trace of other anionic and cationic substitutions after implantation. This study simulated HAp inspired scaffold structure with different anionic and cationic substitutions

to further investigate the effect of substitution on HAp inspired scaffold. Simulations of 0 wt%, 6 wt%, and 13 wt% carbonate substitution cases are used for anionic substitution effect study; simulations of 0 vol%, 5 vol %, and 12.5 vol% magnesium and zinc cases are used for cationic substitutions effects study. Both studies are simulated under 150 N uniaxial compression force. The elastic constants of different degree of substituted HAp are calculated with DFT calculations (Deymer et al., 2017; Aryal et al., 2015). The results of the FEA simulations are shown in Figure 4.2.1.

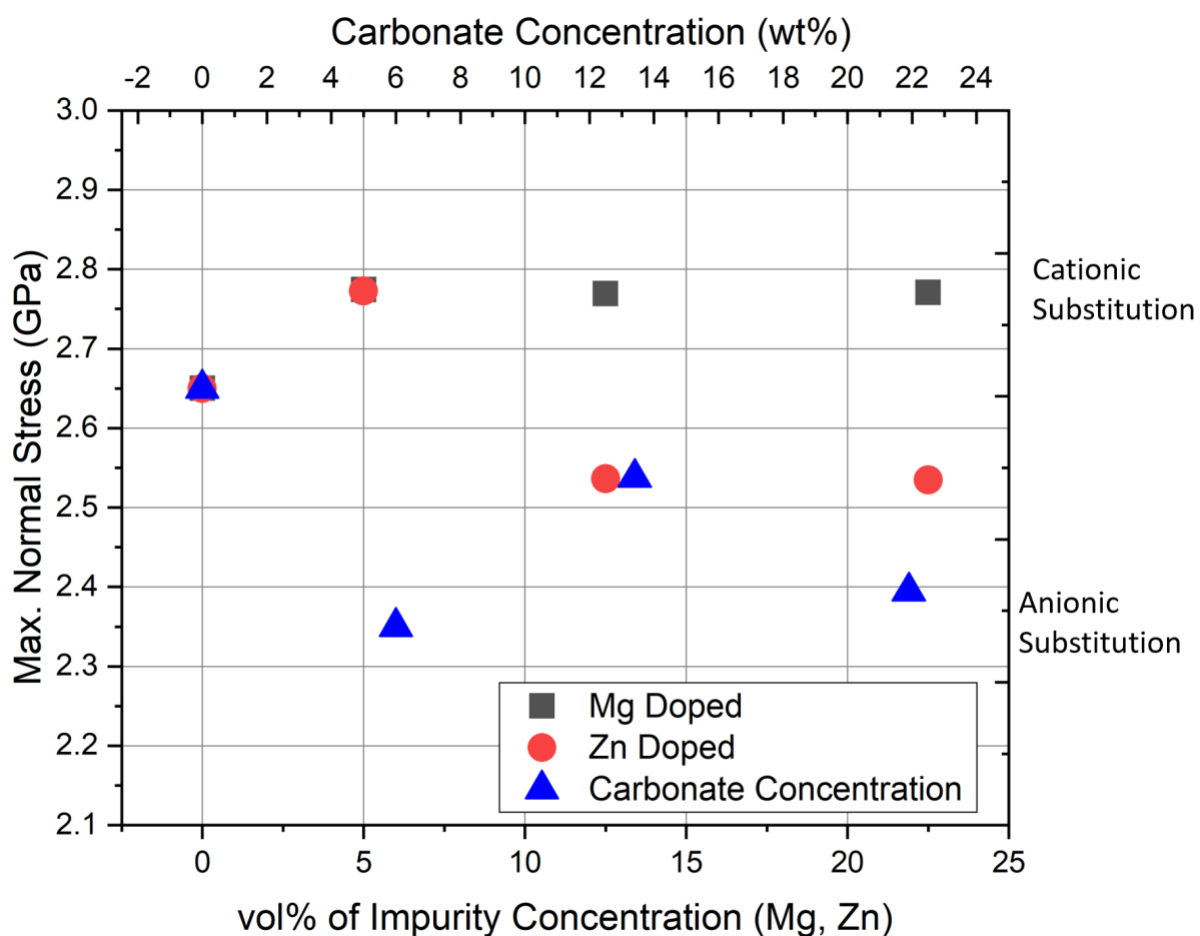


Figure 4.2.1: Maximum normal stress in the loading direction (z-axis) of 0 wt%, 6 wt%, 13 wt%, and 22 wt% carbonated cases are simulated, and 0 vol%, 5 vol%, 12.5 vol%, and 22.5 vol% magnesium and zinc of substituted HAp scaffold under 150 N uniaxial compression. The maximum normal stress is not changing significantly as the level of the cationic substitutions increase. However, for the anionic substitution, the maximum normal stress changed more than 10% even at a lower level of substitution, such as 6 wt%

From this simulation, the effects caused by cationic (Mg^{2+} , Zn^{2+}) and anionic (CO_3) substitutions are different. For the effect of cationic substitutions, the maximum stress on the scaffold is not changing much when the level of substitutions is changing from 0 to 25 vol%. Especially for the magnesium substitution, the maximum normal stress are almost unchanged, about 2.77 GPa, over the changes in the different levels of impurity concentration. For zinc substitution, the range of maximum normal stress is between 2.53 and 2.78 GPa for different levels of substitution. However, the different level of anionic substitution leads to unpredictable change in the maximum stress on the scaffold. This may be caused by the way in which the anionic substitution (CO_3) affects HAp cell's lattice parameters, crystal morphology, and crystallinity, which in turn affects the HAp elastic constants. On the other hand, in the case of cationic substitutions (Mg^{2+} , Zn^{2+}), those substitutions do not affect the lattice structure significantly (Shepherd et al., 2012).

Figure 4.2.1 shows the influence of cationic and anionic substitutions on HAp inspired scaffold. The increasing level of anionic substitution makes the HAp inspired scaffold have a lower maximum normal stress due to decreasing elastic constants. However, the increase of the level of cationic substitution has a minimal effect in lowering maximum normal stress, these effects are due to minimal change in the elastic constants. The effects of anionic substitutions on the stiffness of scaffold are much hard to predict than cationic substitutions. It could change the stiffness and strength on different directions of the scaffold significantly, and potentially make the scaffold more likely to fail under the given loading conditions. Although the effect of both anionic and cationic substitutions in this study is not very significant (~ 10% changes in maximum stress at most), considering the possibility of other different substitutions, the total effects of substitutions on the

elasticity and mechanical strength of scaffolds could still be significant. Thus, the substitutional effect is worth taking into considerations as a factor in bone grafting scaffold designs.

4.3. FEA results of Surface Texture Simulations

In the surface texture study, the primary focus is on the stress level and stress distribution in each surface texture for every simulation case. For this purpose, von Mises stress distribution of every case is plotted and maximum von Mises stresses are also found. A series of comparisons of results is performed to analyze the effects of surface structure shape, coating thickness, spacing distance, and the number of layers on the stress level. The stress level and distribution differences between coating and base are also studied.

The maximum von Mises stress on 10-layer cone surface and hemisphere surface are first compared. For both surfaces, during the simulation, they are under 120 μN loading from the counter face, while the counter face is moving towards the negative x -direction at 5 μm per second. From Figure 4.3.1, the maximum von Mises stress on the coating of the cone surface is much higher than on the hemisphere surface, which is 53.325 MPa and 19.998 MPa, respectively. The maximum von Mises stress on the base of cone surface and hemisphere surfaces are 2.274 MPa and 0.885 MPa, respectively. From the results, the whole cone surface, including the coating and base, is under almost 3 times higher than the maximum von Mises stress during the simulation, which indicates that although cone surface has a lower coefficient of friction, structurally, higher stress would concentrate on it. From Figure 4.3.2, the stress is mostly concentrated on the first few layers of the coating of the cone surface. In contrast, although the stress distribution on the coating of hemisphere surface is also more concentrated on the top three layers, it is much more equally distributed. Higher maximum stress on the cone structure could lead to its surface structure failure sooner than the hemisphere surface. It is also worth noting that for both surface structures, the

stress is more concentrated on the top few layers. This means that these 3D printed layered structures are more likely to fail layer-by-layer rather than by catastrophic collapse.

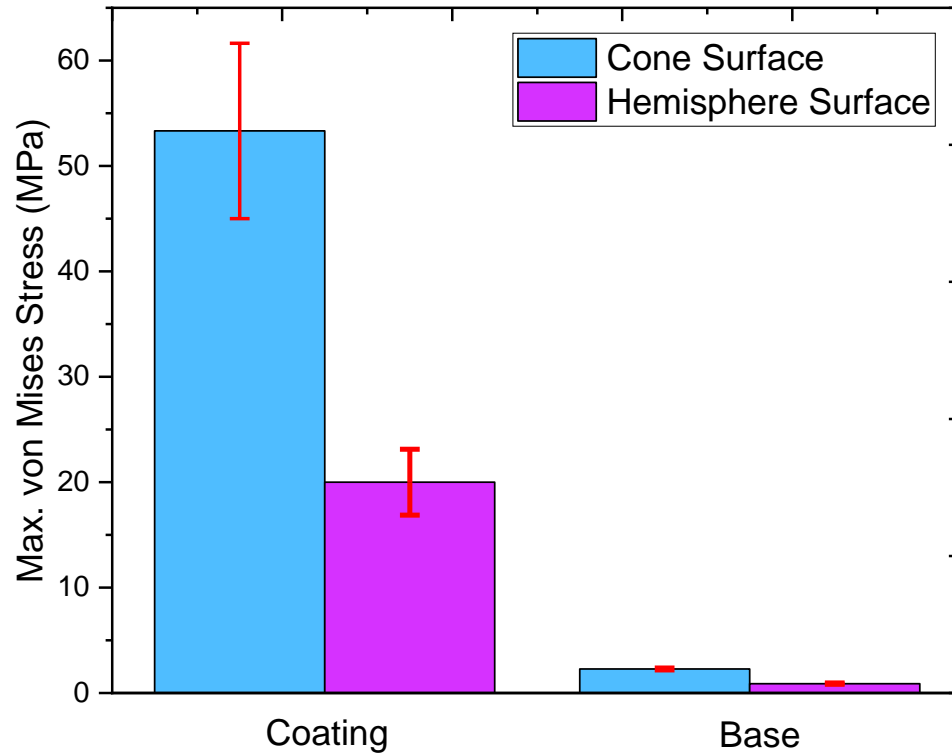


Figure 4.3.1: Maximum stress on 10-layer cone surface and hemisphere surface. The cone surface is under a much larger stress for both coating and base during the simulation. For both surfaces, higher stress is concentrated on the coating.

From Figure 4.3.1 and Figure 4.3.2, there is an obvious difference in stress level between coating and base for both surface structures. The maximum stress on the coatings is about 23 times higher than the maximum stress on the base for both structures. The yield stress of IP-Dip and alumina are 0.125 GPa and 2.906 GPa, respectively. The yield stress of the material of the coating is also about 23 times higher than the material of the base. Although the maximum stress on the coating is much higher than the stress on the base, both coating and the base could fail at the same

time. However, since the IP-Dip base is more like a mold to support alumina coating during the additive manufacturing rather than an actual part of the structure, in the following study, only the coating is discussed.

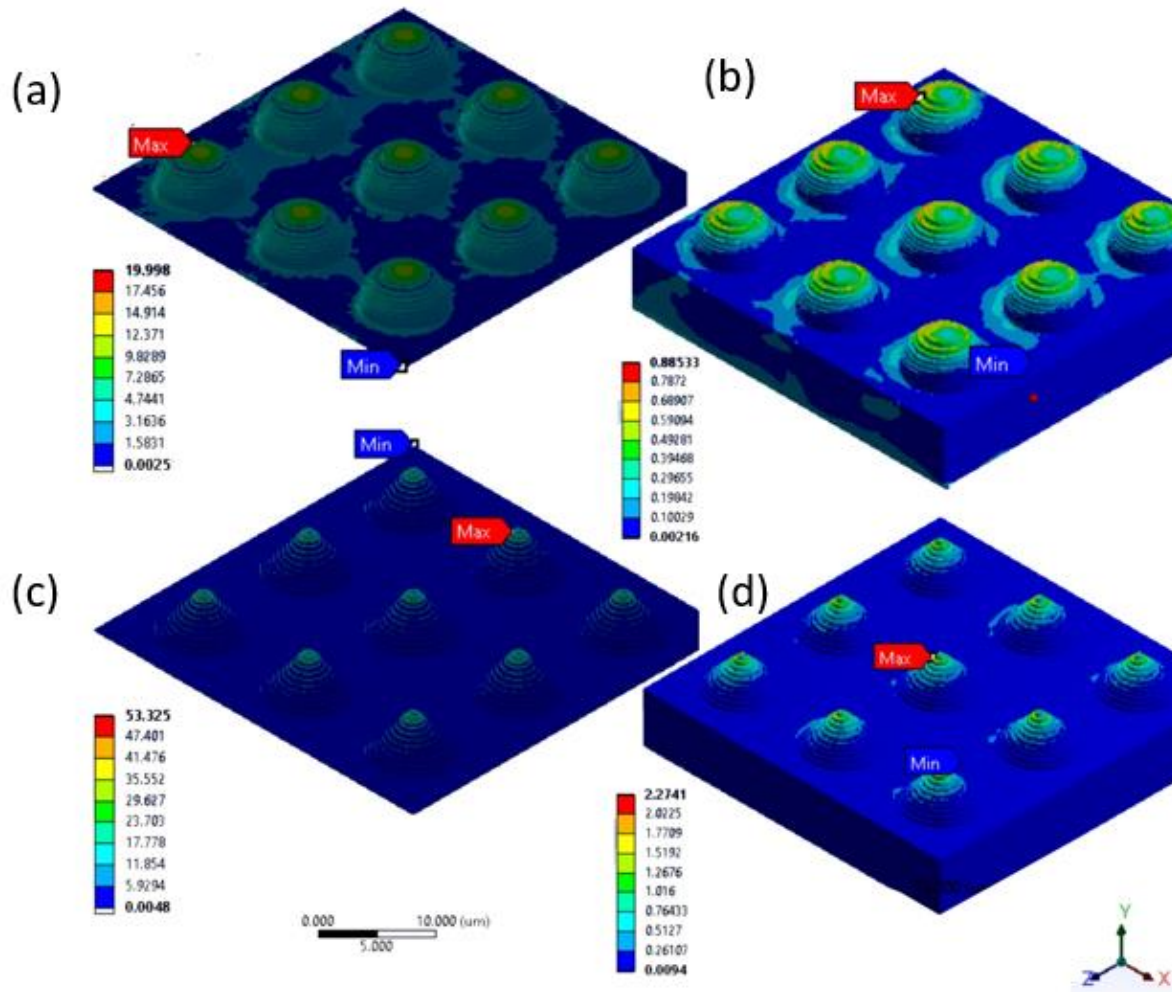


Figure 4.3.2: Stress distribution of 10-layer cone and hemisphere surface during the simulation. (a) Hemisphere coating, (b) hemisphere base, (c) cone coating, and (d) cone base. For both surfaces, the maximum stress locations are on the corner on the top of the second layer; and most stress is concentrated on the top three layers, so the 3D printed layer structures are most likely to fail layer by layer instead of catastrophic structural failure.

The effect of coating thickness is shown in Figure 4.3.3 (a). The coating thickness of cone surface and hemisphere surface are set to 100 nm, 200 nm, and 300 nm. From the results, the

maximum stress on the cone surface is higher than on the hemisphere surface in all three cases, but the differences in maximum stress between two structures are getting closer. The maximum von Mises stress on the cone surface with 100 nm, 200 nm, and 300 nm thickness are 119.75 MPa, 53.325 MPa, and 21.22 MPa, respectively. As the thickness of coating increases, the maximum von Mises stress decreases significantly. For example, at 300 nm thickness the maximum stress is only about 1/6 of the 100 nm thickness case. In contrast, for the hemisphere cases, despite the maximum von Mises stress also decreases as the thickness of coating increases, the difference in the maximum von Mises stress is minor. The maximum von Mises stress of 100 nm, 200 nm, and 300 nm thickness coating are 21.01 MPa, 19.998 MPa, and 19.72 MPa, respectively. This indicates that the high stress level on cone surface is more related to the thickness of the coating than to the structural geometry.

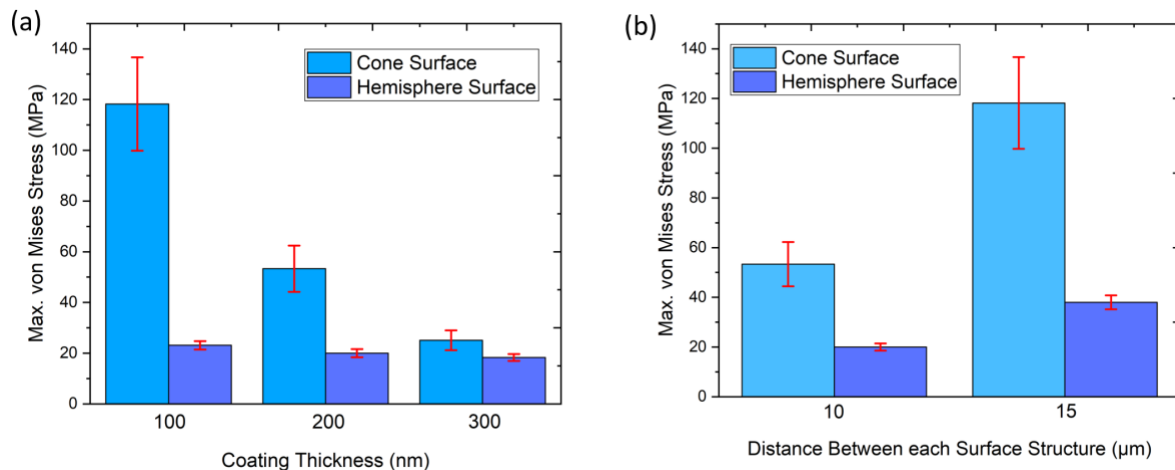


Figure 4.3.3: (a) the effect of coating thickness on maximum stress. For cone surface, as the thickness of the coating increases, the maximum stress on the surface decreases significantly. When the thickness increases from 100 nm to 300 nm, the maximum stress drops 75%. Similar trends appear for the hemisphere surface, but are much less significant. (b) The effect of distance between surface structures on maximum stress. For both surfaces, as surface structures are more spaced out, the maximum stress increases.

The effect of distance between each surface structure for both surfaces are shown in Figure 4.3.3 (b). When the distance between each surface structure increases, the density of surface structures on a surface decreases, which means in a given area of the surface, the number of surface structures will decrease. For both surfaces, the maximum von Mises stress increases as the surface structures space out. For the cone and hemisphere surfaces, the maximum stress increases from 53.325 MPa to 118.95 MPa and from 19.998 MPa to 39.78 MPa, respectively. Based on the results, from the stress reduction perspective, the distance between each surface structure should be as small as possible. However, since other surface properties such as cell adhesion, protein absorption, and coefficient of friction are also affected by the distance between each surface structure, the decision for choosing the parameter distance should be considered carefully based on all factors.

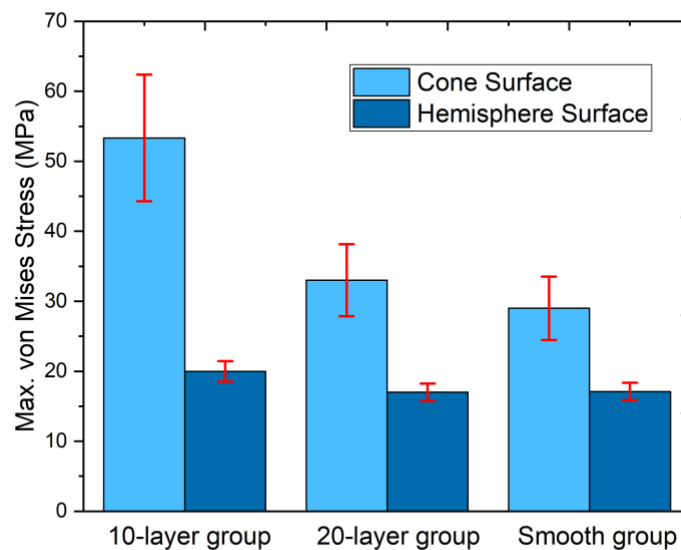


Figure 4.3.4: Comparison of maximum stress among 10-layer group, 20-layer group, and smooth group. Geometrically, a structure with more layers is closer to the ideal smooth structure. The same applies to stress level, the maximum stress on more layered structure appears to be lower and closer to that on the ideal smooth structure.

Due to the limitations of additive manufacturing, although the design of surface structures containing smooth edges, the actual specimens have a layer-by-layer structure. The effect of layer thickness is shown in Figure 4.3.4. For both surfaces, as the number of layers increase their structures become closer to the ideal smooth models, and the maximum stress decreases and gets closer to the maximum stress on the ideal smooth models. The maximum von Mises stress on the cone surface of 10-layer, 20-layer, and smooth structures are 53.325 MPa, 33.25 MPa, and 31.12 MPa, respectively. For the hemisphere cases, the maximum von Mises stress decreases as the number of layer increases as well, the maximum von Mises stress of 10-layer, 20-layer, and smooth structures are 19.998 MPa, 17.65 MPa, and 17.25 MPa, respectively. The changes are more significant in cone surface than the hemisphere surface. The stress difference in the hemisphere surface does not change significantly as the number of layers changes. Due to the nature of 3D printing technique, more layers require more time to print. Thus, the hemisphere surface is ideal for quicker 3D printing with lower precision. In contrast, for the cone surface, a high precision 3D printing can reduce stress concentration on it significantly.

CHAPTER 5: CONCLUSIONS

This study introduced a bio-inspired scaffold for bone grafting based on the geometry features of a HAp unit cell. Unlike most bone grafting scaffolds that are restricted from manufactory limitations, HAp inspired scaffold has a carefully designed pore system, instead of in-line arranged square shaped or the traditional foam-liked structure that is arranged randomly (He, 2008; Hing et al., 2003; Ayers et al., 1999).

Four areas are discussed in this study in terms of the mechanical strength of the porous structures: porosity, pore size, pore shape, and pore arrangement. To achieve high mechanical strength, high porosity, and the large pores required by bone grafting, the HAp inspired scaffold uses carefully designed pore shape and arrangement to overcome some disadvantages that large pore size and high porosity may cause. Large hexagon shaped pores are employed to achieve large pore size and high porosity for bone cell regeneration while retaining structural stability. Meanwhile, a triangular honeycomb-like sandwich structure is employed to increase surface area, porosity, and mechanical strength. Additionally, the effects of substitutions on HAp-made scaffolds are also simulated in this study. Stress reaction of different bio-inspired surface texture designs are also studied.

The following conclusions are determined by simulating the scaffolds in uniaxial compression, biaxial compression, and bending tests:

1. From the uniaxial compressive simulation, a given scaffold structure will have a higher stress level with higher porosity.
2. From the uniaxial compressive simulation results, round pores scaffold and HAp-inspired scaffold both have a relatively low stress level among scaffolds with similar porosity and pore size.

3. The HAp-inspired scaffold has the highest surface area among all scaffolds with similar porosity and pore size.
4. From the bending and biaxial compressive simulations, the HAp-inspired scaffold has the lowest stress level in both cases.
5. To further improve the mechanical strength of HAp inspired scaffold, the staggered pore arrangement pattern is modified into in-line arrangement pattern; as a result, the stress level of the modified HAp inspired scaffold reduced by approximately 16.2% in the uniaxial test. However, the stress level increases by approximately 15.9% in the biaxial test, and only reduced by approximately 6.9% in the bending test.
6. All three substitutions affect elastic constants, with cationic substitution affecting the elastic constants much more significantly than anionic substitutions.
7. The change in stress level on the HAp-inspired scaffold is not significant when the type of substitution is anionic; the change becomes more significant with cationic substitutions.
8. For all cases in the surface texture study, the cone surface always has a higher stress level compared to the hemisphere surface with the same number of layers, coating thickness, or distance between surface structures.
9. For all cases in the surface texture study, the stress level on the coating is much higher than it is on the base.
10. For both surface structures, as the coating thickness increases, the stress levels of both coating and base decrease. This trend is more significant on the cone surface structure than the hemisphere surface structure.

11. For both surfaces, as the distance between each surface structure increases, the stress level increases as well. This trend is more significant on the cone surface than on the hemisphere surface.
12. When the number of layer increases, the geometry of surface structures comes closer to the ideal model. For both surfaces, the stress level decreases as the number of layer increases. This trend is more significant on the cone surface than on the hemisphere surface.

To conclude, the stress level of scaffold structures could decrease significantly by designing carefully and considering several criteria, including pore size, pore shape, and pore arrangement. From this investigation, it is confirmed that the HAp inspired scaffold is able to utilize these designing criteria to offset some negative effects caused by high porosity and large pore size. It also has a large total surface area due to the triangular honeycomb truss design. With a properly designed surface texture, its bone regeneration function could be further enhanced. Therefore, although there are challenges to manufacturing such implants using current techniques, the excellent properties displayed by these bio-inspired structures may make them worth investigating as potential candidates for bone graft scaffold designs.

CHAPTER 6: FUTURE WORK

This study is mostly focused on predicting the stress levels on scaffolds and surface textures under different loading conditions, therefore, bone regeneration experiments are not conducted, which might warrant further study in the future. For the substitution effects, considering the variety of substitutions, each one of them could have a different effect on the elasticity and mechanical strength of scaffolds. Furthermore, substitutions would not only affect elasticity and mechanical strength, but would also affect osteoclastic response, osteoblastic response, thermostability, solubility, degradation, and bone regeneration of scaffolds. Therefore, the substitution effect needs to be considered in scaffold design and should be further investigated.

REFERENCES

- Amini, A. R., Laurencin, C. T., & Nukavarapu, S. P. (2012). Bone tissue engineering: recent advances and challenges. *Critical Reviews™ in Biomedical Engineering*, 40(5).
- Andreiotelli, M., Wenz, H. J., & Kohal, R. J. (2009). Are ceramic implants a viable alternative to titanium implants? A systematic literature review. *Clinical Oral Implants Research*, 20(s4), 32-47.
- Anselme, K., Ploux, L., & Ponche, A. (2010). Cell/material interfaces: influence of surface chemistry and surface topography on cell adhesion. *Journal of Adhesion Science and Technology*, 24(5), 831-852.
- Aryal, S., Matsunaga, K., & Ching, W.-Y. (2015). Ab initio simulation of elastic and mechanical properties of Zn-and Mg-doped hydroxyapatite (HAP). *Journal of the mechanical behavior of biomedical materials*, 47, 135-146.
- Astala, R., & Stott, M. J. (2005). First principles investigation of mineral component of bone: CO₃ substitutions in hydroxyapatite. *Chemistry of Materials*, 17(16), 4125-4133.
- Ayers, R., Wolford, L., Bateman, T., Ferguson, V., & Simske, S. (1999). Quantification of bone ingrowth into porous block hydroxyapatite in humans. *Journal of biomedical materials research*, 47(1), 54-59.
- Balani, K., Verma, V., Agarwal, A., & Narayan, R. (2015). *Biosurfaces: A Materials Science and Engineering Perspective*: John Wiley & Sons.
- Bargmann, S., Scheider, I., Xiao, T., Yilmaz, E., Schneider, G. A., & Huber, N. (2013). Towards bio-inspired engineering materials: Modeling and simulation of the mechanical behavior of hierarchical bovine dental structure. *Computational Materials Science*, 79, 390-401.
- Bose, S., Roy, M., & Bandyopadhyay, A. (2012). Recent advances in bone tissue engineering scaffolds. *Trends Biotechnol*, 30(10), 546-554. doi:10.1016/j.tibtech.2012.07.005
- Brydone, A., Meek, D., & Maclaine, S. (2010). Bone grafting, orthopaedic biomaterials, and the clinical need for bone engineering. *Proceedings of the Institution of Mechanical Engineers, Part H: Journal of Engineering in Medicine*, 224(12), 1329-1343.
- Burchardt, H. (1983). The biology of bone graft repair. *Clin Orthop Relat Res*(174), 28-42.
- Carty, W. M., & Lednor, P. W. (1996). Monolithic ceramics and heterogeneous catalysts: honeycombs and foams. *Current Opinion in Solid State and Materials Science*, 1(1), 88-95.
- Ching, W., Rulis, P., & Misra, A. (2009). Ab initio elastic properties and tensile strength of crystalline hydroxyapatite. *Acta Biomaterialia*, 5(8), 3067-3075.
- Collier, T., Jenney, C., DeFife, K., & Anderson, J. (1997). Protein adsorption on chemically modified surfaces. *Biomedical sciences instrumentation*, 33, 178-183.
- Compton, B. G., & Lewis, J. A. (2014). 3D-printing of lightweight cellular composites. *Advanced materials*, 26(34), 5930-5935.

- Cox, S. C., Thornby, J. A., Gibbons, G. J., Williams, M. A., & Mallick, K. K. (2015). 3D printing of porous hydroxyapatite scaffolds intended for use in bone tissue engineering applications. *Materials Science and Engineering: C*, 47, 237-247.
- Curtis, A., & Wilkinson, C. (1997). Topographical control of cells. *Biomaterials*, 18(24), 1573-1583.
- Derby, B. (2012). Printing and prototyping of tissues and scaffolds. *Science*, 338(6109), 921-926.
- Deymier, A. C., Nair, A. K., Depalle, B., Qin, Z., Arcot, K., Drouet, C., . . . Genin, G. M. (2017). Protein-free formation of bone-like apatite: New insights into the key role of carbonation. *Biomaterials*, 127, 75-88.
- Dimitriou, R., Jones, E., McGonagle, D., & Giannoudis, P. V. (2011). Bone regeneration: current concepts and future directions. *BMC medicine*, 9(1), 66.
- Do, A. V., Khorsand, B., Geary, S. M., & Salem, A. K. (2015). 3D printing of scaffolds for tissue regeneration applications. *Advanced healthcare materials*, 4(12), 1742-1762.
- Eshraghi, S. (2015). *Additive manufacture of tissue engineering scaffolds for bone and cartilage*. Georgia Institute of Technology.
- Frost, H.M. Wolff's law and bone's structural adaptations to mechanical usage: An overview for clinicians. *The Angle Orthodontist* 1994, 64, 175-188.
- Giannozzi, P., Baroni, S., Bonini, N., Calandra, M., Car, R., Cavazzoni, C., ... & Dal Corso, A. (2009). QUANTUM ESPRESSO: a modular and open-source software project for quantum simulations of materials. *Journal of physics: Condensed matter*, 21(39), 395502.
- Gibson, L. J., & Ashby, M. F. (1999). *Cellular solids: structure and properties*: Cambridge university press.
- Hannink, G., & Arts, J. C. (2011). Bioresorbability, porosity and mechanical strength of bone substitutes: what is optimal for bone regeneration? *Injury*, 42, S22-S25.
- He, L.-H., Standard, O. C., Huang, T. T., Latella, B. A., & Swain, M. V. (2008). Mechanical behaviour of porous hydroxyapatite. *Acta Biomaterialia*, 4(3), 577-586.
- Health, U. D. o., & Services, H. (2004). Bone health and osteoporosis: a report of the Surgeon General. *Rockville, MD: US Department of Health and Human Services, Office of the Surgeon General*, 87.
- Hing, K. A., Best, S. M., Tanner, K. E., Bonfield, W., & Revell, P. A. (2004). Mediation of bone ingrowth in porous hydroxyapatite bone graft substitutes. *Journal of Biomedical Materials Research Part A*, 68(1), 187-200.
- Huang, S. H., Liu, P., Mokasdar, A., & Hou, L. (2013). Additive manufacturing and its societal impact: a literature review. *The International Journal of Advanced Manufacturing Technology*, 67(5-8), 1191-1203.
- Hughes, J. M., Cameron, M., & Crowley, K. D. (1989). Structural variations in natural F, OH, and Cl apatites. *American Mineralogist*, 74(7-8), 870-876.
- Huiskes, R. Stress shielding and bone resorption in tha: Clinical versus computer-simulation studies. *Acta Orthop Belg* 1993, 59, 118-129.

- Inzana, J. A., Olvera, D., Fuller, S. M., Kelly, J. P., Graeve, O. A., Schwarz, E. M., . . . Awad, H. A. (2014). 3D printing of composite calcium phosphate and collagen scaffolds for bone regeneration. *Biomaterials*, 35(13), 4026-4034.
- Junqueira, L. C., & Carneiro, J. (2005). *Basic histology text and atlas*: London: McGraw Hill, 2005.
- Karageorgiou, V., & Kaplan, D. (2005). Porosity of 3D biomaterial scaffolds and osteogenesis. *Biomaterials*, 26(27), 5474-5491.
- Kundu, J., Pati, F., Shim, J.-H., & Cho, D.-W. (2014). Rapid prototyping technology for bone regeneration *Rapid Prototyping of Biomaterials* (pp. 254-284): Elsevier.
- Leach, J. K., & Mooney, D. J. (2004). Bone engineering by controlled delivery of osteoinductive molecules and cells. *Expert opinion on biological therapy*, 4(7), 1015-1027.
- Lemma, E. D., Rizzi, F., Dattoma, T., Spagnolo, B., Sileo, L., Quattieri, A., . . . Pisanello, F. (2017). Mechanical properties tunability of three-dimensional polymeric structures in two-photon lithography. *IEEE Transactions on Nanotechnology*, 16(1), 23-31.
- Liu, D.-M. (1997). Influence of porosity and pore size on the compressive strength of porous hydroxyapatite ceramic. *Ceramics International*, 23(2), 135-139.
- Logan, D. L. (2011). *A first course in the finite element method*: Cengage Learning.
- Maggi, A. (2018). *Three-dimensional Nano-architected Materials as Platforms for Designing Effective Bone Implants*. California Institute of Technology.
- Menéndez-Proupin, E., Cervantes-Rodríguez, S., Osorio-Pulgar, R., Franco-Cisterna, M., Camacho-Montes, H., & Fuentes, M. (2011). Computer simulation of elastic constants of hydroxyapatite and fluorapatite. *Journal of the mechanical behavior of biomedical materials*, 4(7), 1011-1020.
- Mironov, V., Trusk, T., Kasyanov, V., Little, S., Swaja, R., & Markwald, R. (2009). Biofabrication: a 21st century manufacturing paradigm. *Biofabrication*, 1(2), 022001.
- Montemayor, L., & Greer, J. (2015). Mechanical response of hollow metallic nanolattices: combining structural and material size effects. *Journal of Applied Mechanics*, 82(7), 071012.
- Moreno, M., H Amaral, M., M Sousa Lobo, J., & C Silva, A. (2016). Scaffolds for bone regeneration: state of the art. *Current pharmaceutical design*, 22(18), 2726-2736.
- Mueller, B. (2012). Additive manufacturing technologies—Rapid prototyping to direct digital manufacturing. *Assembly Automation*, 32(2).
- Müller, B., Riedel, M., Michel, R., De Paul, S. M., Hofer, R., Heger, D., & Grützmacher, D. (2001). Impact of nanometer-scale roughness on contact-angle hysteresis and globulin adsorption. *Journal of Vacuum Science & Technology B: Microelectronics and Nanometer Structures Processing, Measurement, and Phenomena*, 19(5), 1715-1720.
- Murphy, C. M., Haugh, M. G., & O'Brien, F. J. (2010). The effect of mean pore size on cell attachment, proliferation and migration in collagen–glycosaminoglycan scaffolds for bone tissue engineering. *Biomaterials*, 31(3), 461-466.

- Nagels, J.; Stokdijk, M.; Rozing, P.M. Stress shielding and bone resorption in shoulder arthroplasty. *Journal of shoulder and elbow surgery* 2003, 12, 35-39.
- Nair, A. K., Gautieri, A., Chang, S.-W., & Buehler, M. J. (2013). Molecular mechanics of mineralized collagen fibrils in bone. *Nature communications*, 4, 1724.
- Niinomi, M.; Nakai, M. Titanium-based biomaterials for preventing stress shielding between implant devices and bone. *International journal of biomaterials* 2011, 2011.
- Oryan, A., Alidadi, S., Moshiri, A., & Maffulli, N. (2014). Bone regenerative medicine: classic options, novel strategies, and future directions. *Journal of orthopaedic surgery and research*, 9(1), 18.
- Paul, C. D. (2015). *Interface Property of Collagen and Hydroxyapatite in Bone*.
- Pilia, M., Guda, T., & Appleford, M. (2013). Development of composite scaffolds for load-bearing segmental bone defects. *BioMed research international*, 2013.
- Polo-Corrales, L., Latorre-Esteves, M., & Ramirez-Vick, J. E. (2014). Scaffold design for bone regeneration. *Journal of nanoscience and nanotechnology*, 14(1), 15-56.
- Puleo, D., & Nanci, A. (1999). Understanding and controlling the bone-implant interface. *Biomaterials*, 20(23-24), 2311-2321.
- Rechendorff, K., Hovgaard, M. B., Foss, M., Zhdanov, V., & Besenbacher, F. (2006). Enhancement of protein adsorption induced by surface roughness. *Langmuir*, 22(26), 10885-10888.
- Ren, F., Case, E., Morrison, A., Tafesse, M., & Baumann, M. (2009). Resonant ultrasound spectroscopy measurement of Young's modulus, shear modulus and Poisson's ratio as a function of porosity for alumina and hydroxyapatite. *Philosophical Magazine*, 89(14), 1163-1182.
- Ridzwan, M.; Shuib, S.; Hassan, A.; Shokri, A.; Ibrahim, M.M. Problem of stress shielding and improvement to the hip implant designs: A review. *J. Med. Sci* **2007**, 7, 460-467.
- Schijve, J. (2001). *Fatigue of structures and materials*: Springer.
- Shepherd, J. H., Shepherd, D. V., & Best, S. M. (2012). Substituted hydroxyapatites for bone repair. *Journal of Materials Science: Materials in Medicine*, 23(10), 2335-2347.
- Si, L., Wang, X., Xie, G., & Sun, N. (2015). Nano-adhesion and friction of multi-asperity contact: a molecular dynamics simulation study. *Surface and Interface Analysis*, 47(9), 919-925.
- Šupová, M. (2015). Substituted hydroxyapatites for biomedical applications: a review. *Ceramics International*, 41(8), 9203-9231.
- Wahl, L., Maas, S., Waldmann, D., Zürbes, A., & Frères, P. (2012). Shear stresses in honeycomb sandwich plates: Analytical solution, finite element method and experimental verification. *Journal of Sandwich Structures & Materials*, 14(4), 449-468.
- Weis, J. S. (2012). *Walking Sideways: The Remarkable World of Crabs*: Cornell University Press.
- Yang, J. Y. (2006). Pillar Directed Cell Growth. *Imaging & Microscopy*, 8(4), 28-29.
- Zhang, L., Prosser, J. H., Feng, G., & Lee, D. (2012). Mechanical properties of atomic layer deposition-reinforced nanoparticle thin films. *Nanoscale*, 4(20), 6543-6552.

- Zhou, S., Li, Y. B., Wang, Y. Y., Zuo, Y., Gao, S. B., Li, M., & Zhang, L. (2014). The Porous Structure and Mechanical Properties of Injection Molded HA/PA66 Scaffolds. *International Polymer Processing*, 29(4), 454-460. doi:10.3139/217.2851
- Zok*, F. W., Rathbun, H., He, M., Ferri, E., Mercer, C., McMeeking, R. M., & Evans, A. G. (2005). Structural performance of metallic sandwich panels with square honeycomb cores. *Philosophical Magazine*, 85(26-27), 3207-3234.